A waste cryogenic energy assisted freshwater generator for marine applications

Liu, Meixi; Wu, Dawei; Tsolakis, Athanasios; Gao, Wenzhong

DOI:
10.1016/j.desal.2020.114898

Document Version
Peer reviewed version

Citation for published version (Harvard):
Liu, M, Wu, D, Tsolakis, A & Gao, W 2021, 'A waste cryogenic energy assisted freshwater generator for marine applications', *Desalination*, vol. 500, 114898. https://doi.org/10.1016/j.desal.2020.114898

A waste cryogenic energy assisted freshwater generator for marine applications

Meixi Liu [a], Dawei Wu [a,1], Athanasios Tsolakis [a], Wenzhong Gao [b]

[a] *Department of Mechanical Engineering, University of Birmingham, Birmingham B15 2TT, UK*

[b] *Merchant Marine College, Shanghai Maritime University, Shanghai 201306, China*

Abstract

The scarcity of freshwater resources in the marine environment drives advancement of conventional desalination technologies. It is appealing to recover waste thermal energy to power desalination process. With the fast expansion of the global fleet of liquefied natural gas (LNG) powered vessels and the number of LNG terminals, it is envisaged that LNG cryogenic energy becomes an important form of waste thermal energy apart from engine exhaust. A freshwater generator assisted by LNG cryogenic energy is proposed and investigated in the paper. A semi-dynamic model of the proposed system is used to predict performance and optimal parameters. Feed-in seawater, cooling medium, and configurations of the evaporator and the condenser are three key factors to influence the freshwater production rate and required cryogenic energy. The optimal design is able to provide 1021.7 kg/h freshwater from feed-in seawater of 1296 kg/h and LNG evaporation of 3150 kg/h. A scenario study on an LNG powered cruise ferry predicted that freshwater of 16991 kg is generated in the 48-hour voyage with the fluctuating LNG cryogenic energy from evaporation, which varies between 212 kW and 973 kW.

Keywords: LNG cryogenic energy; freshwater generator; thermal distillation; flash evaporation.

Nomenclature

Letters

A	convective heat exchange area, m^2
a_i	constant value of Nusselt Number
d	hydraulic diameter, m
E	relative error
Ex	exergy, kW
h	enthalpy, kJ/kg
k	convective heat transfer coefficient, W/ ($m^2 \cdot K$)
km	mass transfer coefficient, W/ ($m^2 \cdot K$)
Hv	latent heat of vaporization, kJ/kg
L	moist air channel gap, m
Le	Lewis number
l	characteristic length, m
m	mass, kg
$\dot{m}$	mass flow rate, kg/s
M	mass of per unit area, kg/m^2
P	pressure, bar
$\dot{Q}$	sum of the heat flow rates entering or leaving the volume, kJ
q	heat flow rate, kJ/kg
R	perfect gas constant, J/ ($kg \cdot K$)
T	temperature, K
t	time, s
U	internal energy, kJ
u	internal energy per unit of mass, kJ/kg
V	volume, m^3
v	specific volume, m^3/kg

Subscripts

[1] Corresponding author email address: d.wu.1@bham.ac.uk

0	environment temperature
aw	water vapour in the moist air
b	brine
ch	channel
da	dry air
d	exergy destruction
e	experimental
f	fresh water
fr	frost
i	inlet
lw	liquid water
lam	laminar flow
ma	moist air
o	outlet
s	simulation
sat	saturation condition
s	seawater
t	theoretical
$turb$	turbulent flow
v	water vapour
w	wall

Greek letters

ρ	density, kg/m^3
λ	thermal conductivity, W/ (m · K)
δ	thickness, m
φ	absolute humidity, kg/kg$_{dry}$

Abbreviations

EPR	Exergy Performance Ratio
FWG	Freshwater Generator
FD	Freeze Desalination
GOR	Gained Output Ratio
HDH	Humidification-Dehumidification
LNG	Liquefied Natural Gas
MED	Multi-effect Distillation
MSF	Multi-stage Flash Distillation
MVC	Mechanical Vapour Compression
Nu	Nusselt Number
PR	Performance Ratio
Pr	Prandtl Number
PVDF	Polyvinylidene Fluoride
Re	Reynolds number
RO	Reverse Osmosis
RR	Recovery Ratio
SCD	Single-stage Conventional Distillation
SD	Solar Distillation
TDS	Total Dissolved Solids
TVC	Thermal Vapour Compression

1. *Introduction*

Freshwater is one of the essential elements of life on earth. Although 70% of the earth is covered by water, the vast majority of this is seawater containing 30,000-40,000 ppm of total dissolved solids (TDS), which is not suitable for human direct consumption [1]. Desalination technologies remove salts and minerals within seawater, thereby providing a solution of producing freshwater in marine environment, coastal countries and archipelago areas where there is a scarcity of freshwater resources.

In general, desalination technologies are mainly classified into two types: thermal distillation and membrane desalination. Sophisticated thermal distillation technology includes Single-stage Conventional Distillation (SCD), Multi-stage Flash Distillation (MSF), Multi-effect Distillation (MED), Mechanical Vapour Compression (MVC), Thermal Vapour Compression (TVC) and Solar Distillation (SD). Membrane desalination includes Reverse Osmosis (RO), Electrodialysis and Membrane Distillation. Apart from these technologies, Freeze Desalination (FD) and Humidification-Dehumidification (HDH) are also proved to be workable technologies to obtain freshwater in small scales. Important performance data of these desalination technologies are shown in Table 1.

Table 1 Summary of desalination technologies [2]**.**

	SCD [3]	**MSF**	**MED**	**MVC**	**TVC**	**SD**	**RO**	**FD**	**HDH[4]**
GOR (kg/kg) *	0-1	8-12	10-16	N/A	12	~0.5	N/A	N/A	-
PR (kg/MJ) **	0.9	3.5-5.25	4.35-6.9	N/A	4.4	-	N/A	N/A	1.1
Thermal energy consumption (MJ/m^3)	214.25	190-282	146-229	N/A	174	Solar passive	N/A	N/A	-
Electricity consumption of pumps or others (kWh/m^3)	-	2.5-5.0	2.0-2.5	7.0-12.0	1.6-1.8	-	3.5-6.0	-	-
Water recovery rate	28%	10%-15%	20%-35%	40%	40%	20-46%	<55%	<53%	2%
TDS (ppm)	<10	<10	<10	<10	<10	<10	200-500	<500	<500
Typical plant size (m^3/day)	-	50,000 - 70,000	5,000 - 15,000	100-3,000	10,000-30,000	<100	<128,000	-	-
Water costs ($/$m^3$)	20 [5]	0.6-1.8	0.5-8.0	0.9-2.6	0.9-2.6	1.3-6.5	0.3-13.0	0.34	19

*GOR (kg/kg): the gain output ratio, the ratio of the mass of distillate (kg) to the mass of the input steam (kg).
**PR (kg/MJ): the performance ratio, the ratio of the mass of distillate (kg) and input heat.

Considering economic and technical factors, most of deepsea vessels use freshwater generators (FWGs) to meet freshwater requirement rather than storing a large quantity of freshwater in tanks. Among the technologies, several types systems are prevalent to be used as FWGs in marine applications, i.e. SCD, MSF, MED and RO [6]. Although RO accounts for more than 60% installed desalination plants around the world, it is easily affected by feed-in seawater quality, inherent problems of relatively high ppm TDS in produced freshwater, high energy/chemical consumption, and high operational and maintenance costs [7]. Researchers have been exploring new RO designs, especially with novel membranes with advantageous properties [8]. Compared to complicated designs of MSF and MED, SCD, especially low-pressure SCD is considered as the best choice for FWG marine applications due to its simple design, lower maintenance cost, better freshwater quality, waste energy recovery potential and compact size [9]. However, SCD is hindered by its limitations [5], i.e. the higher input energy consumption and lower freshwater recovery rate of 20% to 30%, which attracts further research interests to reduce energy consumption and promote freshwater recovery rate. Several approaches are proposed, e.g. employment of flash evaporation process, improvement of condensation efficiency, and utilization of renewable energies.

Flash evaporation is widely investigated, which refers to when a liquid enters a large chamber with a pressure drop below its saturation pressure, rapid vaporization happens along with temperature drop [10]. Flashing process provides a higher vaporization speed under low-pressure conditions than a simple boiling process. Low pressure conditions draw water saturation pressure decreasing significantly as well as corresponding water saturation temperature. Low grade heat with temperature in the range of 40℃ to 80℃ becomes feasible to be employed for flash evaporation, which results in a good cost-saving on energy consumption. Initial operation conditions and fluid state are the key influential factors of flash evaporation process. Saury, et al. [11] proved that the flash evaporation process is reinforced with higher superheat degree through water film experiments. El-Fiqi, et al. [12] explored that with the inlet temperature increasing from 40 to 70 ℃, the evaporated mass rate is increased by 57%. And the flash efficiency is intensified from 0.75 to 0.95. Abbaspour, et al. [13] designed a natural vacuum system with solar evacuated tube collectors which proves that the increased vacuum level improves the water production and system efficiency. Fathinia, et al. [14] investigated that when injection pressure decreased from 6 bar to 0.25 bar, the evaporation rate is increased by at least 66.7%. Furthermore, flash evaporation process is also influenced by inlet feed water mass flowrate, nozzle diameter, injection direction and relative humidity reported by Miyatake, et al. [15], Ikegami, et al. [16] and Chen, et al. [17].

Condensation efficiency is equally important to affect energy consumption and freshwater production rate [18]. A few research have indicated that an ultra-low temperature cooling source has a great potential to improve condensation efficiency freshwater production and reduce heating energy consumption [19]. An ultra-low temperature source of liquefied natural gas (LNG) evaporation is firstly investigated as a cooling source for FWGs, which is readily available from LNG regasification on LNG powered vessels and LNG terminals. During regasification of LNG at -162 ℃ under atmospheric pressure, about 830 kJ/kg cryogenic energy will be released [20]. Depends on sizes of ship engines, several MW cooling energy could be released from LNG powered vessels, which may increase to several thousand MW scales at LNG terminals with regasification infrastructures [21]. The proposed FWG system also has increasing applications with the growing number of LNG powered ships reported by DNV GL [22], especially large passenger vessels, with the co-location demands for clean emissions and large quantity freshwater supplies. The fast-growing number of LNG terminals and regasification infrastructures near harbour areas of coastal megacities, e.g. Singapore, Shanghai, etc. may further create potential FWG applications co-located with vast LNG cryogenic energy source. As condensation happens at the cryogenic temperature in the proposed FWG, highest temperature in evaporation can be largely decreased to a low grade heating temperature level (lower than 70 ℃), which broadens the choice of low-temperature waste heat sources and reduces high grade thermal energy consumption. However, the application of LNG cryogenic energy in desalination technologies may bring some issues, e.g. the frosting/freezing phenomena occurring on the gas-solid interface, which will influence heat transfer performance and block the vapour flow.

Although LNG is firstly considered for marine related applications of FWG based on thermal distillation desalination technologies, its cryogenic energy was widely investigated in FD, a novel desalination technology to extract freshwater from saline water through ice crystals with nearly zero power consumption. Research on FD can date back to 1977, when Cravalho, et al. [23] proposed a net-zero work theoretic system utilizing cryogenic energy generated by a heat engine and a heat pump for ice production and desalination. The theoretical maximum freshwater output was 6.75 kg water/kg regasified LNG. Cao, et al. [24] designed an indirect freeze desalination plant with LNG to lower the temperature of the refrigerant R410A. The FD prototype designed by Lin, et al. [25] proved that LNG is feasible to assist FD process, but the salt removal rate is only 50%. FD is also coupled with other technologies used in hybrid desalination systems, e.g. hybrid indirect-contact freeze desalination-direct contact membrane distillation process [26] and RO-freeze process [27]. LNG cryogenic energy could also be recovered to minimise the energy consumption in another desalination technology, the hydrate-based desalination process. In this process, the cold energy is required for hydrate formation and crystal separation. He, et al. [28] proved that clathrate hydrate-based desalination process by utilizing LNG cryogenic energy obtains higher water recovery rate and less energy consumption compared with FD process. The lower cost of water in its economic evaluation report with employed LNG indicates that the hydrate-based process is a potential solution to increase the freshwater supply in LNG regasification infrastructures [29]. Babu, et al. [30] introduced the possibility of applying the technology for commercial use and achieved the maximum salt rejection rate at 87.5%.

This study firstly proposes to integrate flash boiling in vacuum condition of evaporator, and LNG cryogenic energy recovery into the widely used marine FWGs (using SCD technology), which has a great potential to reduce overall energy use in marine FWGs, increase water recovery ratio, and maintain high quality of drinkable freshwater with low TDS. An analytic model of the proposed new FWG are firstly described in detail and validated by experimental literatures, which provides a quantitative means to predict its performance compared to traditional counterparts or other competitive technologies. A further parametric analysis is carried out to maximise freshwater production. A first case study of the proposed FWG system on a cruise ferry is analysed to predict freshwater yield, energy saving and LNG cryogenic energy recovery. This provides a crucial evidence for the reference of researchers and industry looking into novel FWG technologies assisted with LNG, a primary marine fuel in next couple decades.

2. *Configuration of a cryogenic energy assisted FWG*

An innovative desalination system assisted by LNG cryogenic energy is illustrated in Fig. 1. The system consists of an evaporation chamber, a feed-in seawater tank, a compact condenser and pumps. Seawater from the tank is injected into the evaporation chamber which maintains a low pressure created by a vacuum pump. In the evaporation chamber, a portion of the heated feed-in seawater is evaporated to generate vapour and the rest is drained off at the bottom as brine. LNG from the fuel storage tank is pumped through the condenser and regasified to natural gas to absorb a large amount of heat. The generated vapour from the evaporator enters the condenser to be condensed to freshwater with the cold energy from LNG.

The flash evaporation chamber and the condenser in the system are developed and optimised by numerical method. Two submodels of the evaporation chamber and the condensor are built in Siemens Simcentre AMESim and validated with the experimental results from the references. The optimisation of the system is conducted to identify influential factors such as pressure, temperature, mass flow rate and configuration of heat exchangers. The performance of the proposed system is estimated based on the freshwater production and recovery rate (RR). A comparative study between the proposed system and a conventional desalination system is carried out. And the condensate and heat transfer performance is also explored considering the frost formation on the cryogenic surface. Finally, the proposed system is put into a scenario case in which LNG fuel consumption data of a case vessel is used as input to predict freshwater production.

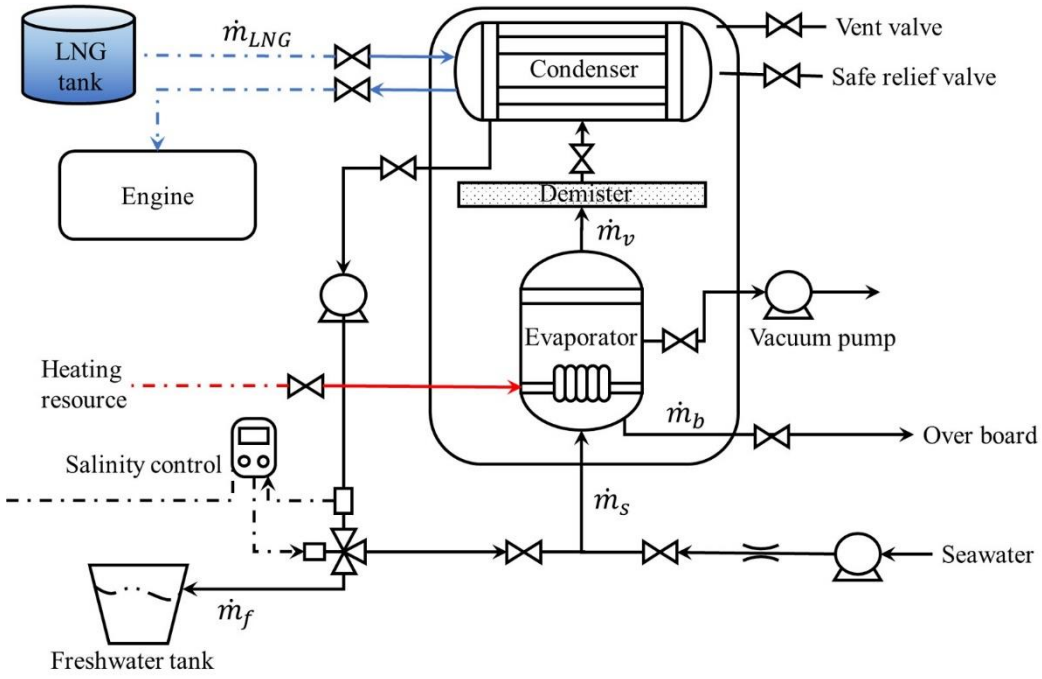

Fig. 1. Schematic of the proposed system.

3. Modelling of the proposed FWG

3.1 The governing equations

The modelling of a flash evaporation chamber and a compact condenser in the proposed FWG is based on the following assumptions:
(1) A control volume of the evaporator chamber is selected to develop the balance of mass and energy,
(2) There is no entrainment of mist by the vapour, and the vapour is salt-free,
(3) Due to low pressure, the working fluid is regarded as an ideal gas,
(4) Heat transfer between the evaporator chamber/the condenser and the environment is negligible,
(5) The vacuum in the evaporation chamber and the condenser can be maintained throughout,
(6) The flow of non-condensable gas is negligible,
(7) The vapour and minor quantity air existing in the system is considered as the moist air.
(8) The consumed energy of pump and valves are negligible compared to the thermal energy.

According to the assumptions, the mass balance and the energy balance in the flash evaporator chamber are given as:

$$\dot{m}_s = \dot{m}_b + \dot{m}_v \tag{1}$$

$$\dot{m}_b h_b + \dot{m}_v h_v = \dot{m}_s h_s + \dot{Q} \tag{2}$$

The time derivative of the density of the feed-in seawater is given by the mass conservation law in the evaporation chamber as follows:

$$\frac{d\rho}{dt} = \frac{1}{V} \cdot \sum \dot{m} \tag{3}$$

The internal energy based on the first law of thermodynamics is expressed as:

$$\frac{dU}{dt} = \sum \dot{m} \cdot h + \dot{Q} \tag{4}$$

After simplification of Eq. (3) and Eq. (4), the temperature of the feed-in seawater can be expressed by the following equation:

$$\frac{dT}{dt} = \frac{1}{m \cdot c_v} \cdot \left(\sum \dot{m} \cdot h + \dot{Q} - h \cdot \sum \dot{m} - m \cdot \left(P + \frac{\partial u}{\partial v}|_T \right) \cdot \frac{dv}{dt} \right) \tag{5}$$

where P is the pressure in the chamber, the value is determined using the Maxwell relation as:

$$\frac{dP}{dt} = \frac{\partial P}{\partial v}|_T \cdot \frac{dv}{dt} + \frac{\partial P}{\partial T}|_v \cdot \frac{dT}{dt} \tag{6}$$

According to the assumptions above, the mass balance and the energy balance in the compact condenser are given as follows:

$$\dot{m}_{ma} = \dot{m}_v + \dot{m}_{da} + \dot{m}_{aw} \tag{7}$$

$$\dot{m}_f = \dot{m}_v + \dot{m}_{aw} \tag{8}$$

$$\dot{m}_v h_{v(sat)} + \dot{m}_{LNG,i} h_{LNG,i} = \dot{m}_f h_{f(sat)} + \dot{m}_{LNG,o} h_{LNG,o} \tag{9}$$

When the condensation occurs in the condenser, the water vapour is condensed at the condensation temperature and the phase changes from vapour to the liquid. During this process, the heat energy provided consists of the latent heat of phase change and the sensible heat of temperature reduction. The heat flow rate between the air and the wall during this process is given as:

$$q = k_{ma} \cdot A \cdot \left(T_{ma,i} - T_w \right) + \dot{m}_f \cdot Hv \tag{10}$$

where $T_{ma,i}$ is the inlet moist air temperature; and k_{ma} is the convective heat transfer coefficient of the moist air side, the value is determined by the Nusselt Number (Nu), the thermal property of the moist air and the characteristic length of the exchange as follows:

$$k_{ma} = \frac{\lambda \cdot Nu}{l} \tag{11}$$

The quantity of Nu depends on the type of moist air flow [31]:

$$Nu = \begin{cases} Constant; (laminar\ flow\ with\ constant\ surface\ temperature\ or\ heat\ flow) \\ 0.023 Re^{0.8} Pr^{0.4}; (turbulent\ flow;\ Re \geq 10{,}000, 0.7 \leq Pr \leq 160) \\ Nu_{lam} \cdot \left(1 + \frac{1}{10 \cdot ln(2)} \cdot ln\left(1 + exp\left(10 \cdot ln(2) \cdot \frac{Nu_{turb} - Nu_{lam}}{Nu_{lam}}\right)\right)\right); (transition\ flow) \end{cases} \quad (12)$$

And the characteristic length l depends on the size of the moist air channel gap (when the width is negligible compared to the height) as follows:

$$l = 2L \quad (13)$$

The condensate generated in the condenser during this process is gauged based on the inlet absolute humidity and the outlet absolute humidity:

$$\dot{m}_f = \dot{m}_{da} \cdot (\varphi_i - \varphi_o) \quad (14)$$

The outlet temperature of the moist air after condensation is determined by the inlet conditions and the heat transfer between the moist air and the wall:

$$T_{ma,o} = T_{ma,i} + \frac{q}{q_{max}}(T_w - T_{ma,i}) \quad (15)$$

Similar to the outlet temperature of the moist air, the outlet absolute humidity after condensation is expressed as :

$$\varphi_o = \varphi_i + \frac{q}{q_{max}}(\varphi_w - \varphi_i) \quad (16)$$

where q_{max} is the maximum heat transfer between the wall and the moist air. It is expressed as:

$$q_{max} = \frac{\dot{m}_{ma}}{1 + \varphi_i} \cdot ((1 + \varphi_{sat}) \cdot (h_{ma,i} - h_{ma,w,sat}) + (\varphi_{ma,i} - \varphi_{w,sat}) \cdot (h_{ma,i} - h_{lw,w,sat})) \quad (17)$$

where $h_{ma,w,sat}$ is the moist air specific enthalpy at wall saturation conditions and $h_{lw,w,sat}$ is the liquid water specific enthalpy at wall saturation conditions.

With the cooling medium LNG entering the channels inside the wall, the internal convective heat exchange occurs between the inside wall and the cooling medium. The heat flow rate between the cooling medium LNG and the wall is expressed as:

$$\mathrm{q} = k_{co} \cdot \mathrm{A} \cdot (T_{LNG} - T_{w,LNG}) \quad (18)$$

where k_{co} is the convective heat transfer coefficient between the LNG and the wall, $T_{w,LNG}$ is the inside wall temperature. And the convective exchange surface of the channel A is calculated by:

$$A = \frac{4A_{ch} \cdot l_{ch}}{d_{ch}} \quad (19)$$

where A_{ch} is the cross-sectional area of the channel, l_{ch} is the length of the whole channel and d_{ch} is the hydraulic diameter of the channel which depends on the type of the channel.

In addition, the heat exchange of conduction between the walls should be taken into consideration due to the temperature difference between both sides and the material of the wall. Therefore, the heat flow rate of conduction is referred as:

$$q = \frac{\lambda_w A_w}{\delta}(T_{w,ma} - T_{w,LNG}) \quad (20)$$

where δ is the thickness of the wall and λ_w is the thermal conductivity of the material.

In the evaporator model, the variables are pressure, seawater flow rate, seawater inlet temperture and the heating resource, while in the condensation process, the condensate is the key indicator which varying with the varaibles including the mass flow rate, relative humidity and temperature of inlet moist air, initial pressure in the condenser, cooling medium temperature and mass flow rate. Different

geometry parameters of the condenser such as the heat exchange area and the materials are also considered as variables in the parametric analysis of the following section to identify the maximum freshwater production, i.e. maximum condensate.

The performance of the proposed FWG-LNG system is evaluated by such parameters: water recovery rate (RR), gained output ratio (GOR) and exergy performance ratio (EPR). Water recovery rate (RR) represents the recovery ability of the desalination plant which is the ratio of recovery freshwater to the feed-in seawater [1], as shown below:

$$RR = \frac{\dot{m}_f}{\dot{m}_{sw}} \times 100\% \tag{21}$$

Gained output ratio (GOR) also indicates the performance of the proposed system which is defined as the ratio of the equivalent evaporative energy of the distillate to the external heating input to the evaporator chamber as followed [32]:

$$GOR = \frac{m_f Hv}{Q} \tag{22}$$

Exergy is defined as the maximum theoretical work obtained from the whole system, and it can be destroyed in thermal systems [33]. Based on the second law of thermodynamics, the exergy balance of the whole system can be found as:

$$Ex_i - Ex_o = Ex_d \tag{23}$$

The exergy input of each component is found in Eq. (24) [32].

$$Ex_i = Q \times (1 - \frac{T_0}{T_Q}) \tag{24}$$

In this study, the environment state is defined as 20°C and 1 bar. The exergy performance ratio (EPR) of the system is defined as the output freshwater exergy to the input exergy Ex_i in Eq. (25) .

$$EPR = \frac{Ex_f}{Ex_i} \times 100\% \tag{25}$$

The surface of the condenser may maintain the temperature lower than the freezing point of water vapour, considering the LNG operation temperature. Frost formation occurs when water vapour goes through the plates. In the waste cold energy recovery applications of LNG regasification, frosting is always a critical issue. Excessive frost formation on heat exchanger surface increases thermal resistance and reduces heat transfer coefficient. Therefore, a simple frost formation model with the assumption that the frost on the surface is uniform across the condenser surface is proposed to predict the frost thickness performance. The frost layer thickness can be calculated by the mass of frost per unit area and the frost density from the following equation:

$$\delta_{fr} = \frac{M_{fr}}{\rho_{fr}} \tag{26}$$

Due to the phase change between the water molecules in the water vapour and the cryogenic surface during the frosting process, the mass flux can be obtained from the mass transfer coefficient and the water vapour density at ambient conditions and at frost surface as:

$$\frac{dM_{fr}}{dt} = km(\rho_{v,ma} - \rho_{v,fr}) \tag{27}$$

where the mass transfer coefficient km is calculated based on the Chilton-Colburn analogy [34]:

$$km = \frac{k_{ma}}{\rho_{ma} c_{p,ma} Le^{2/3}} \tag{28}$$

where Le is the Lewis number, defined as the ratio of the thermal diffusivity to mass diffusivity.

3.2 Validation

The experimental data from a few literatures [35,36,37,38] were used to validate the accuracy of the evaporator model and the condenser model developed in Siemens Simcenter Amesim. Appendix A presents the detailed experimental data and the comparison with simulated results. Relative error

(Eq.(29)) between the experimental value and simulation value is used to evaluate the operation performance.

$$E = \frac{\dot{m}_e - \dot{m}_s}{\dot{m}_s} \tag{29}$$

Rahman, et al. [35] proposed a single-effect desalination unit consisting of a submerged vertical tube evaporator and a cooling water tank. The vapour production rate is the key indicator of the evaporator performance. The condensation experimental data obtained by Wu and Vierow [36] and Cheng and Geld [37] are employed on the condenser model to predict the coolant outlet temperature and the condensate. The errors between the numerical model results and the experimental data are within 17%. In addition, the comparison between the experimental and calculated frost layer thickness is explored with the experiments investigated by Lee and Ro [38]. It can be found that all the numerical data agree very well with the experimental data.

4. Results and discussion

The validated evaporator and condenser model are now employed in the proposed FWG system to examine the impact of operational parameters, e.g. mass flow rate, temperature, pressure, etc., and the geometry parameters, i.e. material and heat exchange area. Considering the ultra-low LNG operation temperature, the frosting performance is analysed, and the anti-frosting method is introduced to prevent the frosting harm to heat transfer. A case study on a cruise ferry and a comparative analysis with other desalination technologies is carried out based on the parametric optimisation results.

4.1 Impact of operational parameters

As discussed in the validation part, the superheat and inlet feed-in seawater temperature have an obvious effect on the evaporated mass. Moreover, the influences of other parameters including feed-in seawater mass flow rate, temperature, initial pressure in the chamber and heating input are studied. The different parameters data used to examine are described in Table 2 as Case 1 and Case 2.

Table 2 Operational parameters of the evaporator.

Case	Pressure (bar)	Heating input (W)	Temperature of feed-in seawater (℃)	Mass flow rate of feed-in seawater (kg/s)
1	0.08	12156	31.5, 41.5, 51.5, 61.5	0.01, 0.03, 0.0694, 0.1, 0.13, 0.16
2	0.03, 0.05, 0.08, 0.15, 0.20	0, 4052, 8104, 12156, 16208	61.5	0.0694

Fig. 2 presents how feed-in seawater temperature affects the water vapour mass distribution under different mass flow rates and temperature of feed-in seawater. The initial pressure and heating input are fixed at 0.08 bar and 12156 W. The varying inlet temperature and the mass flow rate conditions are shown as Case 1 in Table 2. It can be found that the water vapour mass flow rate is increased with the increase of the feed-in seawater temperature which implies that the flash evaporation process is enhanced. This phenomenon is attributed to the different superheat degrees. According to the introduction in the previous section, the superheat degree is related to the inlet feed-in seawater temperature under the same pressure of the chamber. With the higher superheat degrees, the vaporization heat absorbed from the liquid itself is higher which results in a faster flash speed and decrease its own temperature to the saturation temperature. Therefore, the flash evaporation process is enhanced with higher superheat degrees.

When the feed-in seawater temperature is pre-heated higher than 41.5 ℃ (saturation temperature at 0.08 bar), the water vapour mass presents an increasing trend. The larger mass flow rate of feed-in seawater corresponds to a larger flow velocity through a fixed size of the inlet component which results in larger evaporated mass with the same heating input. When the feed-in seawater temperature is pre-heated to 41.5 ℃, the superheat degree is 0, the water vapour production remains almost the same when the feed-in seawater mass flow rate increases. The explanation is that the heating input roughly balances with the required latent heat to evaporate the amount of the feed-in seawater at the saturation temperature. Although more feed-in seawater is available when the flow rate increases, no more spare heat is available to evaporate seawater to increase the water vapour production rate. And when the feed-in

seawater temperature is lower than the vapour saturation temperature, the water vapour production rate decreases due to a large portion of the heating input being used to increase the sub-cooling seawater temperature to the saturation temperature. Depending on the availability of waste heat temperature grade, feed-in seawater temperature level is set. Therefore, the initial evaporator chamber pressure can be adjusted accordingly to make feed-in seawater temperature higher than the saturation temperature at chamber pressure.

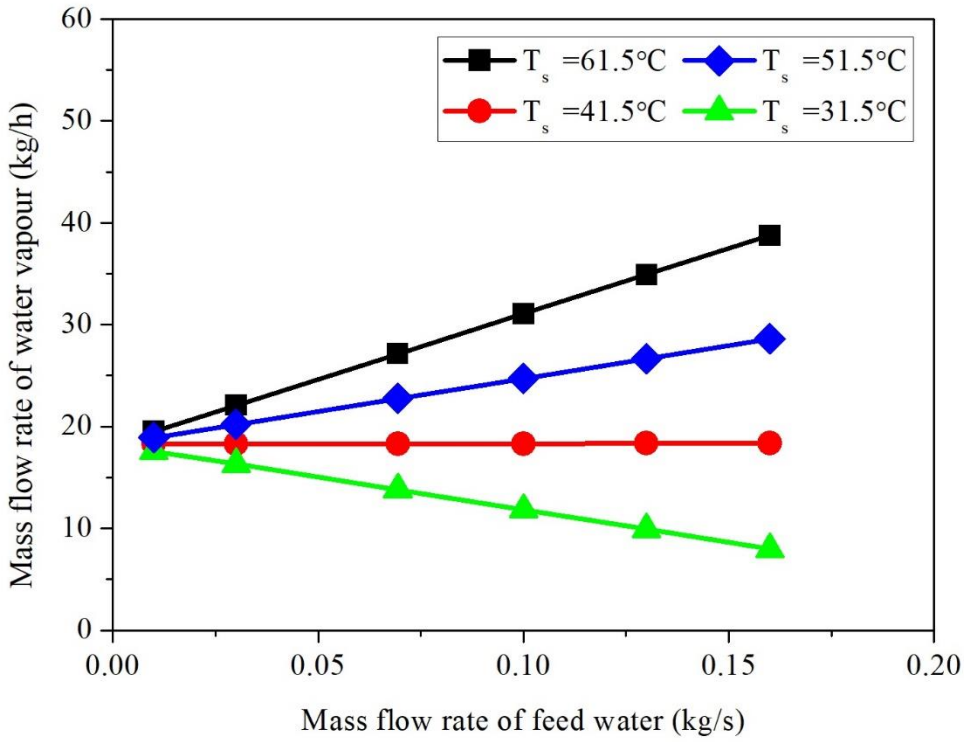

Fig. 2. Variation of water vapour mass with different feed-in seawater temperature in Case 1.

Fig. 3 presents the water vapour production rate versus initial chamber pressure, while five different heating inputs varying from 0 W to 16208 W applied. The operation parameters are described as Case 2 in Table 2. It is clear that the water vapour production rate will increase when the heating input rises. The heating input drives flashing evaporation of the feed-in seawater and increases the flashing speed. Similar results are generated from the evaporator validation result in which the water vapour production rate rises when the superheat degree increases. It is also clear to conclude from Fig. 3 that with the rise of the initial pressure in the evaporation chamber, the water vapour production rate presents a declining trend. Lower initial pressure enhances flashing evaporation process and is associated with lower vapour saturation temperature which augments temperature difference with the feed-in seawater temperature. Thus, there is spare heat energy for generating more vapour in flashing evaporation.

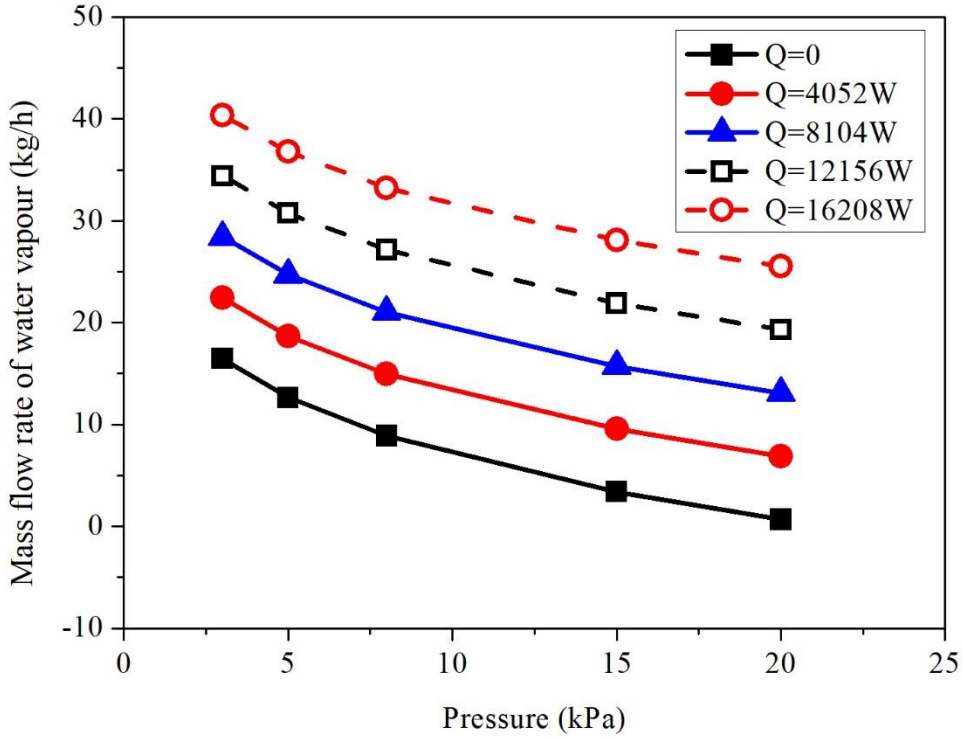

Fig. 3. Variation of freshwater mass with the heating input in Case 2.

Similarly, the performance of the condenser is studied by applying different operational parameters, i. e. mass flow rate, relative humidity and temperature of inlet moist air, initial pressure in the condenser, cooling medium temperature and mass flow rate as described in Table 3.

Table 3 Operational parameters of the condenser.

Case	Pressure of moist air (bar)	Temperature of moist air (℃)	Relative humidity of moist air	Mass flow rate of moist air (kg/s)	Cooling medium temperature (℃)	Cooling medium mass flow rate (kg/s)
3	1	90	40%	0.25	0, 5, 15, 25	0.1, 0.25, 0.4, 0.694, 1, 1.3
4	0.05, 0.08, 0.15, 0.20	30, 40, 50	40%	0.25	5	0.694
5	0.05, 0.08, 0.15, 0.20	40	20%, 30%, 40%, 50%, 60%	0.25	5	0.694
6	0.05, 0.08, 0.15, 0.20	30	40%	0.05, 0.1, 0.15, 0.25, 0.4, 0.694, 1, 1.3	5	0.694

Fig. 4 depicts the condensate produced versus the mass flow rate of cooling medium at different temperatures: 0 ℃, 5 ℃, 15 ℃, 25 ℃ and the other parameters are shown as Case 3 in Table 3. At a constant cooling medium temperature, the condensate flow rate increases with the increasing cooling medium mass flow rate at first, and then approaches its upper limit. Beyond a certain point of the cooling medium mass flow rate, there is only a very limited increase in condensate produced. The reason for this is that a high cooling medium flow rate provides a greater cooling capacity for condensation, which increases the condenser efficiency. However, the constant moist air flow rate is not great enough for a higher cooling medium flow rate with extra cooling capacity to be condensed which directly impacts

heat recovery of condensation. In Fig. 4, it is also noteworthy that with the lower cooling medium temperature, the more condensate is generated. A lower cooling medium temperature is effectively a lower dew point for condensation process which provides a great potential to decrease absolute moisture content in moist air with certain relative humidity. Consequently, the optimal cooling medium working conditions can be selected in terms of an economic mass flow rate and a practically achievable low temperature. Furthermore, this result also applies to the lower temperature of inlet LNG in the future section.

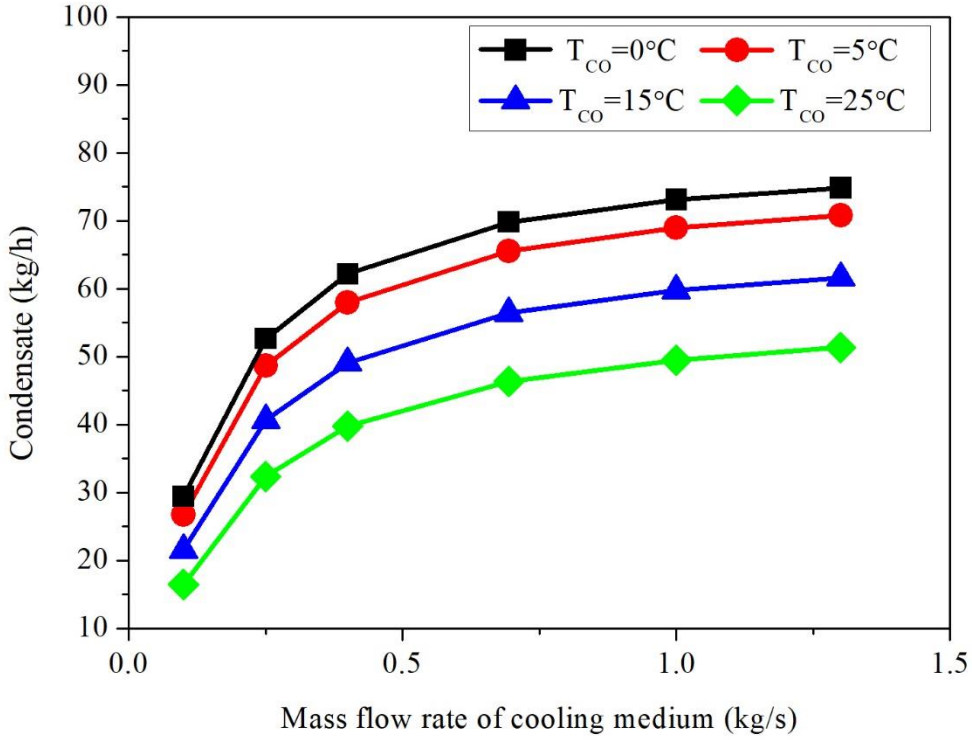

Fig. 4. Variation of condensate with cooling medium temperature in Case 3.

In Case 4 and Case 5, all parameters are listed in Table 3. It can be observed from Fig. 5 and Fig. 6 that the condensate increases with an increase of the temperature and the humidity of moist air, which represent the simulation results of Case 4 and Case 5. The moist air in Case 4 with a relative humidity of 40% and the mass flow rate of 0.25 kg/s is condensed by the cooling water of 0.694 kg/s under 5 ℃ and the other parameters are described in Table 3. The moist air in Case 5 with a temperature of 40 ℃ and the mass flow rate of 0.25 kg/s is condensed by the same cooling water condition. When the pressure in the condenser chamber is 0.05 bar, the condensate is increasing by 73% from the 10.8 kg/h generated by 30 ℃, 40% moist air to 39.6 kg/h generated by 50 ℃, 40% moist air in Fig. 5. With the same pressure in the chamber, the condensate is increasing by 87% from 5.11 kg/h generated by 40 ℃, 20% moist air to 39.6 kg/h generated by 40 ℃, 60% moist air. It is understandable that water vapour in moist air has a higher partial pressure with higher temperature and higher relative humidity of moist air. Therefore, condensate starts to be generated at a relatively higher condensing temperature, which leads to higher condensate production rate.

In Fig. 5 and Fig. 6, it is also observed that the condensate drops by around 50% when the pressure increases from 0.03 bar to 0.20 bar at the temperature of 30 ℃ and the lower relative humidity level of moist air. The reason is that lower pressure results in the lower partial pressure of vapour, in turn, saturation temperature, or dew point. As the geometry of the condenser is unchanged in this comparison, moisture content after the condensation process will be lower with a lower dew point. Therefore, moisture loss, in other words, condensate production is higher with lower pressure in the chamber.

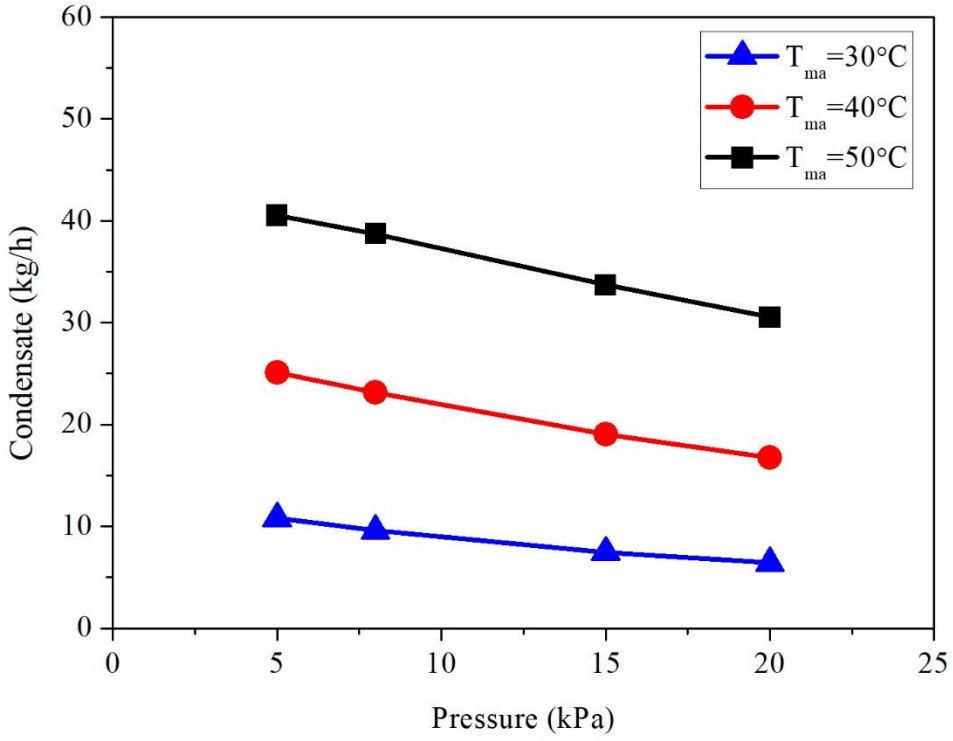

Fig. 5. Variation of condensate with moist air temperature in Case 4.

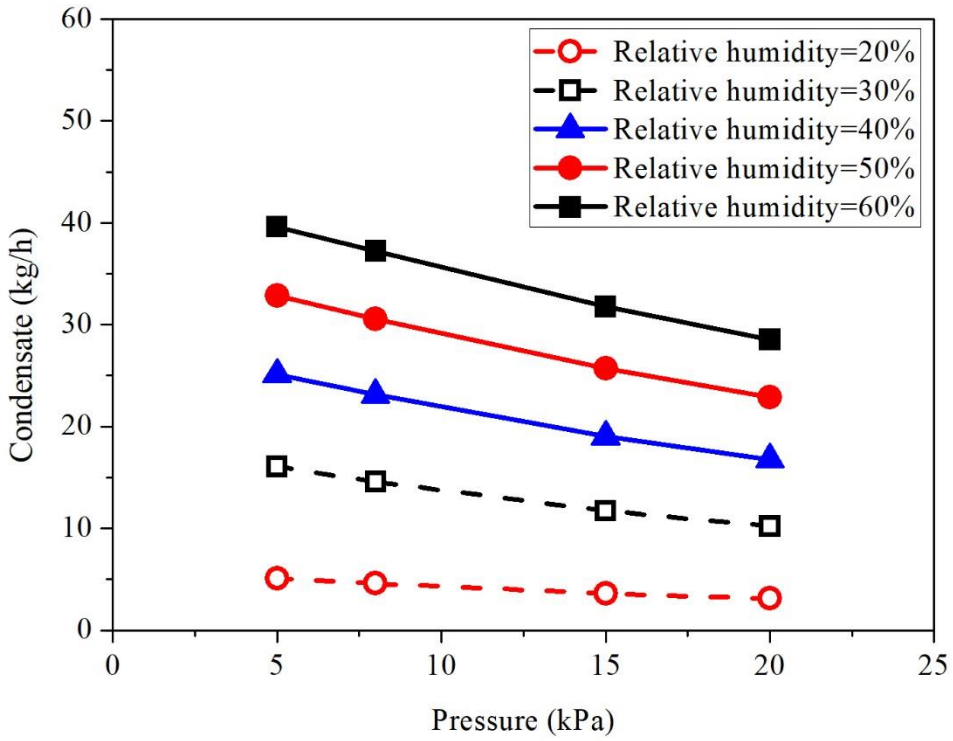

Fig. 6. Variation of condensate with moist air relative humidity in Case 5.

The Case 6 discusses the impact of moist air flowrate and condenser pressure. Fig. 7 shows the condensate under a varying mass flow rate of moist air and pressure in Case 6 with the operational

parameters shown as Case 6 in Table 3. Under a fixed pressure, condensate production rate increases with higher moist air flow rate before it reaches its limitation and then decreases gradually. It is clear that a higher moist air flow rate brings more moisture content for condensation and more cooling energy is needed to balance condensation heat. Additionally, excessive moist air mass flow rate may reduce the heat exchanger effectiveness of the condenser and directly affect cooling energy transfer to facilitate the condensation process. The optimal moist air flow-rate may be obtained by considering conflicting effects.

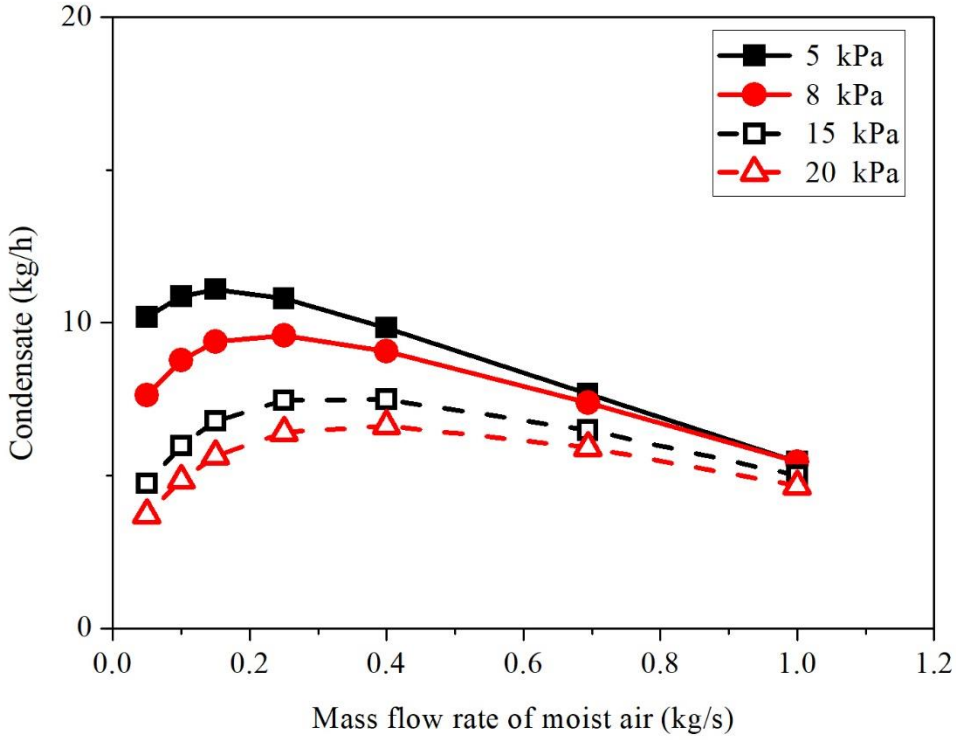

Fig. 7. Variation of condensate with a moist air flow rate in Case 6.

4.2 Impact of geometry parameters on the condenser performance

It has already been demonstrated that the flashing evaporation process is related to the feed-in seawater condition, the heating input and the vacuum condition in the evaporation chamber. And the capacity of the heating input can be obtained from large amounts of free waste heat. Although the configuration of the evaporator can be optimised, it has limited impact on the condensate production rate. However, as the LNG cryogenic energy has been applied as the cooling medium in the new FWG system, and the condensation process is related to the variations of the heat exchanger structure and configuration, the geometry parameters of the condenser are simulated and analysed.

The geometry parameters of the condenser may affect the performance as well as the usability of the condenser when LNG is used as the cooling medium directly. The compact heat exchanger is used to achieve a large heat transfer surface of the condenser, which consists of arrays of plates with flat tubes in 3 passes. Moist air flows across the plates from the first pass to the third pass where it exchanges heat with the cooling medium LNG. The schematic of the condenser is shown in Fig. 8. In this section, the most influential geometry parameters are analysed to evaluate their impact on the performance of the proposed system as shown in Table 4. The moist air is simulated at the pressure of 0.08 bar, temperature of 41.5 ℃, relative humidity of 80.3% mass flow rate of 1.5 kg/s. Two possible LNG inlet conditions, i.e. 1 bar, -162℃ (low pressure LNG storage condition); and 5 bar, -138℃ (high pressure LNG storage condition) are examined. The condensate production rate and the outlet LNG temperature are considered as the main indicators of the system performance.

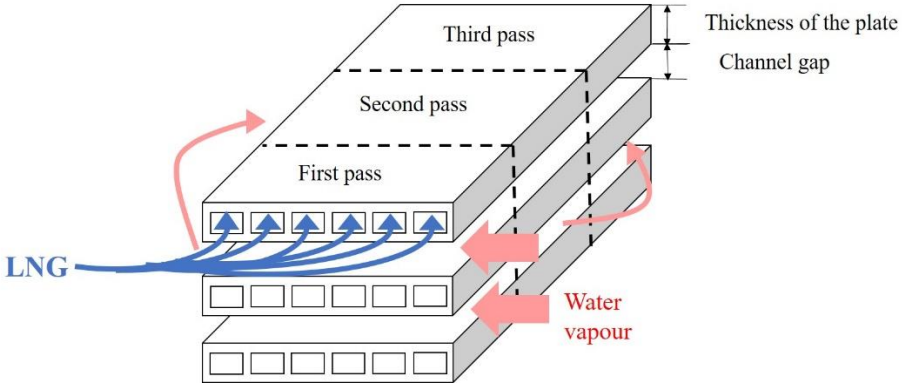

Fig. 8. Details of the proposed condenser for the FWG system.

Table 4 Operational parameters of the moist air and LNG in condenser.

Parameter	Unit	Quantity
Pressure of the condenser	bar	0.08
Temperature of the moist air	℃	41.5
Relative humidity of the moist air	-	80.3%
Mass flow rate of moist air	kg/s	1.5
Pressure of LNG	bar	1, 5
Temperature of LNG	℃	-60, -162, -138
Mass flow rate of LNG	kg/s	0.875

As described in Eq. (20), the conduction heat transfer is related to the thickness of wall material and the thermal conductivity of the material. Fig. 9 shows the outlet LNG temperature (the inlet LNG temperature is -60 ℃ at 1 bar, a typical LNG storage condition before dual fuel engines on board ships) and the condensate production rate affected by different wall materials: i.e., PVDF, Stainless Steel AISI304 and Aluminium Alloy 3003-H14 at the same operational conditions as mentioned as Case 7 in Table 5. When the material has a lower thermal conductivity, the heat conduction flux is lower within the same duration, which results in less cooling energy from LNG transferred into the condenser and the outlet LNG temperature still be in cryogenic temperature. However, with a similar outlet LNG temperature, the condensate results in the Case 7 is very similar when different materials of the condenser, i.e., Stainless Steel AISI304 with thermal conductivity of 16.2 W/ (m · K) and Aluminium Alloy 3003-H14 with thermal conductivity of 159 W/ (m · K) are used. The reason for this is that with the same duration time and the same condenser configuration, the heat exchange area is sufficient for Stainless Steel AISI304 to transfer the applicable LNG cryogenic energy for condensation although its lower thermal conductivity. Consequently, the smaller amount of cryogenic energy for the condensation leads to the less condensate, which can be clearly viewed from Fig. 9. Therefore, due to the better performance and inexpensive cost, Aluminium Alloy 3003-H14 is considered as the best material of the condenser for this application, among the materials considered.

Table 5 Geometry parameters of the condenser.

Case	Heat exchange area of plate (m^2)	Characteristic length of the exchange (mm)	Heat exchange area of the channel (m^2)	Thickness of the plate (mm)	Number of plates	Material of the condenser
7	1.4	4	4.581	0.265	48	Aluminium Alloy 3003-H14; PVDF; Stainless Steel AISI304
8	1.4	4	1.091	0.1, 0.265, 0.45	48	Aluminium Alloy 3003-H14
9	1.4	4	1.091, 2.181, 3.272, 4.581, 5.453	0.265	48	Aluminium Alloy 3003-H14
10	0.368, 0.552, 0.92, 1.4, 1.84	4	1.091	0.265	48	Aluminium Alloy 3003-H14

11	1.4	3, 4, 5, 6	4.581	0.265	48	Aluminium Alloy 3003-H14

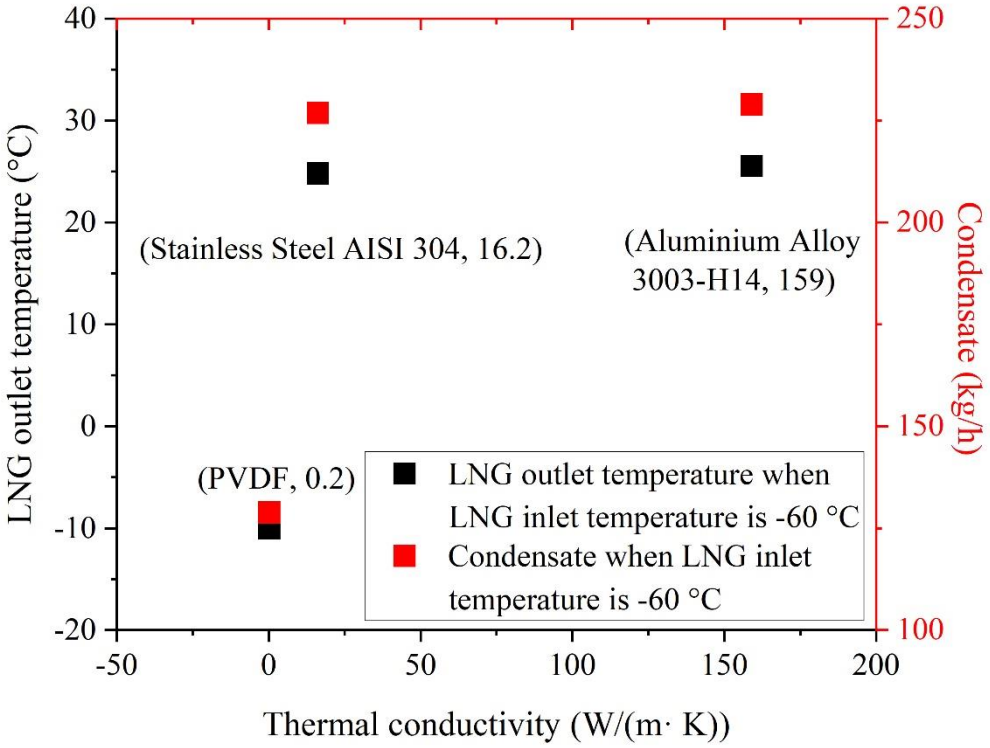

Fig. 9. Variation of condensate with different material in Case 7.

The geometry parameters will affect heat transfer process in the condenser, resultant condensate and required capacity of LNG cryogenic energy. In this section, several parameters of the condenser are discussed, i.e., wall thickness (Case 8), configuration of the channel (Case 9) and the plate (Case 10) and characteristic length of the condenser (Case 11).

Fig. 10 shows the influence of the wall thickness of the condenser on the condensate and the LNG outlet temperature when the inlet LNG temperature is -138 ℃ at 5 bar and -162 ℃ at 1 bar. The configuration parameters of the condenser are presented as Case 8 in Table 5. It is observed that the wall thickness of the condenser has little influence on the condensate and the LNG outlet temperature. With the wall thickness of the material increasing from 0.1 mm to 0.45 mm, the condensate and the outlet LNG temperature changes by 1kg/h. The good performance of Aluminium Alloy 3003-H14 in the condenser reduces the influence of the wall thickness on the heat conduction process over the same duration time. As a result, the smaller thickness of the wall is preferable for condenser design.

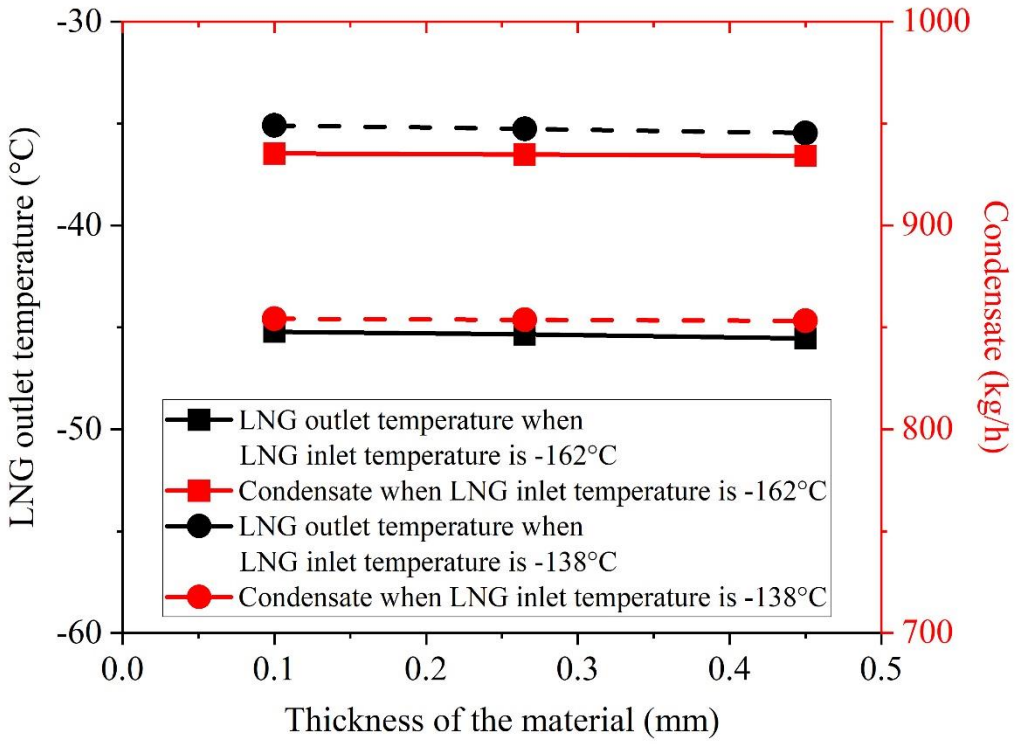

Fig. 10. Variation of condensate with the thickness of the material in Case 8.

Fig. 11 depicts the condensate and the outlet temperature of LNG under varying convective exchange areas of the channels inside the plate. The convective heat exchange area of the channel is varied by increasing the A and B of the channel from 483 mm^2 to 2416 mm^2 and the decreasing the number of channels in each plate from 50 to 10. The results shown in Fig. 11 are based on the steady state values after the simulation runs after 30 minutes. Under the same conditions shown as Case 9 in Table 5, the condensate and the LNG outlet temperature demonstrate an increasing trend as the heat exchange area of channels increases. With the same volume of condenser, the increasing heat exchange area of the channels provides a more efficient area for condensation which promotes the condenser efficiency. Additionally, significantly more capacity of LNG cryogenic energy is transferred and consumed between the cooling medium LNG and the walls to increase the freshwater production rate.

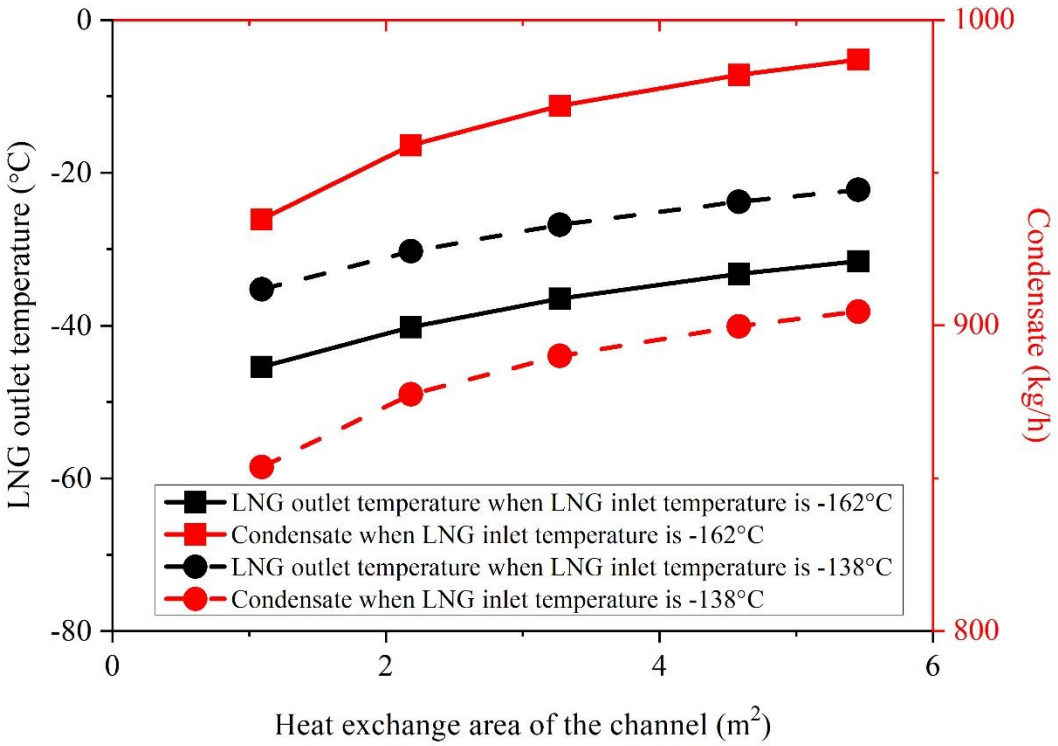

Fig. 11. Variation of condensate with convective exchange area of the channel in Case 9.

Fig. 12 shows the impact of the plate heat exchange area on the condensate and the outlet temperature of LNG. The width of the condenser varies from 20 mm to 100 mm which results in the plate heat exchange area varying from 0.368 m^2 to 1.84 m^2. The other parameters are fixed, as presented as Case 10 in Table 5. The condensate and the LNG outlet temperature present a increase trend with an increasing plate heat exchange area. The reason is that with an increasing plate heat exchange area, the heat transfer between the outer wall and the moist air is enhanced by the transfer of more LNG cryogenic energy. However, the condensate starts to become constant when the exchange area of the plate is more than 1.4 m^2. When the width of the condenser increases, a portion of the moist air has been condensed by the LNG in the first few channels and the temperature drops. This lower temperature moist air will be condensed by the same temperature of LNG in the latter channel with a lower efficiency which reduces the condensation speed. Consequently, the optimal heat exchange area of the plate is the precondition of the higher efficiency and lower cost.

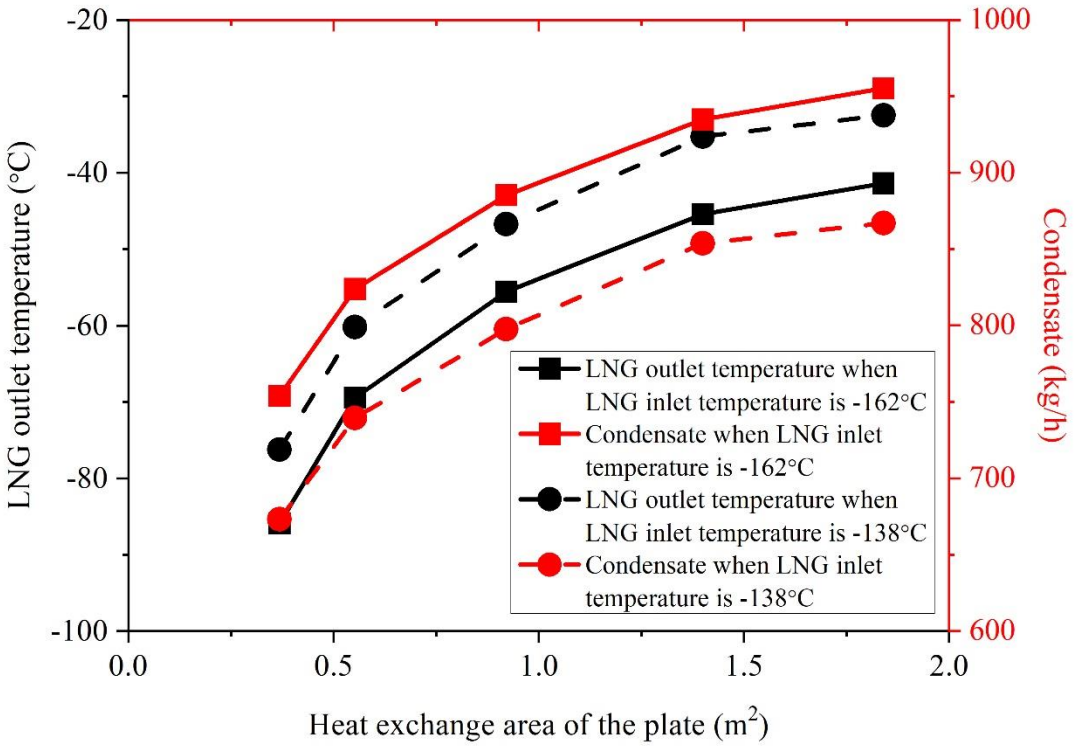

Fig. 12. Variation of condensate with convective exchange area of the plate in Case 10.

Fig. 13 presents the condensate and the outlet LNG temperature under various characteristic lengths of the moist air channels in the condenser. The characteristic length of the condenser is varying with the moist air channel between two plates from 3 mm to 6 mm according to Eq. (13) while the other operational parameters are fixed as presented as Case 11 in Table 5. The optimal condensate is observed to be progressively lower for a higher characteristic length of the condenser. And the condensate with a varying characteristic length of the heat exchanger in the first 20 s is shown in Fig. 14. The condensate increases rapidly in the first few seconds and then decreases to the equilibrium condition. The time spent for the greater moist air channel gap to achieve equilibrium is less than the smaller moist air channel gap. The reason of this phenomenon is that when the moist air starts entering the condenser, the initial moist air will be condensed by the LNG at an extremely low temperature which results in a rapid condensation. As more moist air enters, the system achieves an equilibrium condition. As the moist air channel gap increases, contact factor of the condenser is decreased as there is more moist air not in contact with the surface of the heat exchanger plate. Therefore, it reduces the cooling energy transferred into the moist air from LNG in the plate channels, and the time spent on achieving an equilibrium condition accordingly.

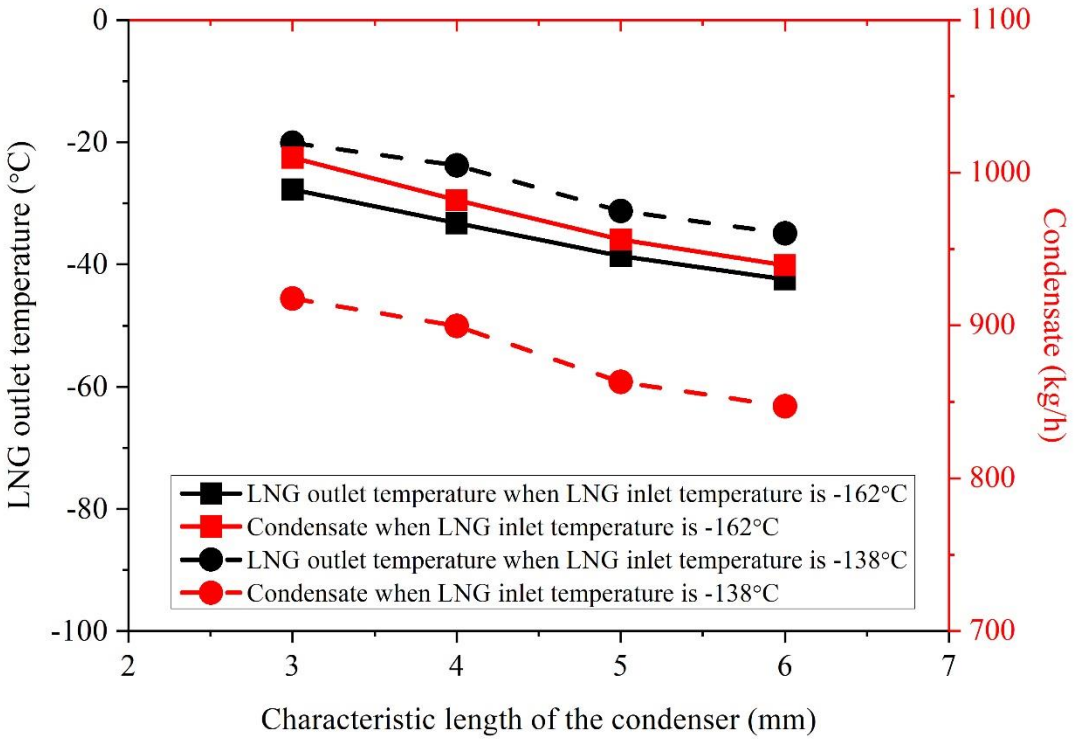

Fig. 13. Variation of condensate with a characteristic length of the condenser in Case 11.

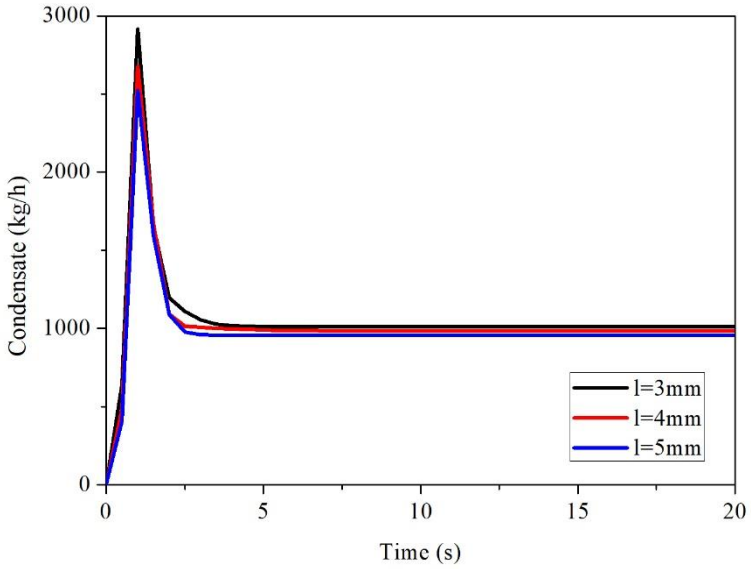

Fig. 14. Variation of condensate with characteristic length in the 20s.

4.3 Frosting influence

As demonstrated above, heat transfer is getting worse as frost formed on cryogenic surface as insulation along the time, which has negative influence in numerous cryogenic industrial fields such as air-conditioning, aerospace field, aviation field and LNG. Frost thickness is affected by surface temperature and moist air conditions i.e. temperature, relative humidity and velocity [39]. Among these, surface temperature is the main influence factor [40], which is also demonstrated in the results of the model in

examination. The system model considering extra frost layers may reveal the degree of performance degradation after certain time.

Fig. 15 compares the system performance between the system model with-frost model and no-frost model including temperature, condensate and frost thickness along the whole heat exchanger tube. It is obvious that both of the wall surface temperature and the condensate leads a higher trend in no-frost model than the with-frost model. It is believed that when frost layer formed on the surface, the thermal conductivity of frost layer (<1 W/m·K) is much less than the surface material (159 W/m·K), which results in exacerbated poor heat transfer, in turn, less condensate. And the thickest frost is obtained at the beginning of the tube because of the lowest LNG operation temperature. As the LNG regasification processing along the tube, the frost formation is weakened with less frost contributed.

The frost formation on the surface restricts the operation of the heat exchanger, thus several methods are employed to defrost such as switch operation time. A second identical heat exchanger unit is made available to allow the primary unit to defrost for minimum 4 hours [40]. Another method is to change the surface structure. According to the mechanism of condensation and desublimation, the frosting process is related with the Gibbs free energy which is determined by the surface temperature and the contact angle of the surface [41]. When contact angle is more than 90°, a surface with hydrophobic or superhydrophobic characteristics provides a higher energy barrier which delays and retards the frosting process [42]. Ji, et al. [43] experimented that the heat transfer performance on the superhydrophobic aluminium tube was improved by 105% than the bare aluminium tube. The frost mass change rate on the superhydrophobic surface presents the slowest trend compared to the untreated and superhydrophilic surface [44]. A comparison experiment between the superhydrophobic surface and bare surface on frosting delay time were proposed by Kim, et al. [45]. They found that the frosting delay time on superhydrophobic surface could be maximum 1200s which is around 300% higher than that of bare surface. The research results above have proved that the superhydrophobic surface heat exchanger presents a feasible method to decrease the frost accumulation, delay the frost formation and improve the heat transfer performance under cryogenic conditions. Furthermore, the superhydrophobic surface reduces required defrosting time and total cycle time [44].

Several methods are investigated to obtain superhydrophobic property based on coating and etching technique such as chemical etching, fluoride coating, sandblasting etching and laser ablation [46]. Ji, et al. [43] used self-assembled monolayer method to fabricate aluminium tubes by immersing in sodium hydroxide and a solution of n-hexane and heptadecafluoro-1,1,2,2-tetrahydrodecyltrichlorosilane, which results in a contact angle of 166° on surface. In the study of Boyina, et al. [44], aluminium substrate is treated by heptadecafluorodecyltrimethoxy-silane toluene solution, acetone and ethanol presents a contact angle at 156°. Different metal substrates utilize different treatment solutions based on their own chemical properties. In the paper of Lu, et al. [47], Ti substrates as anodes and copper plate as cathode were placed in NaBr solution for electrochemical etching to obtain a surface contact angle of 158°. For brass alloy, a mechanical micro-machining process can be applied to fabricate small groove on substrate surface with a cut depth of 12.5 μm to create a contact angle of 140° [48]. The research on the hydrophobic and superhydrophobic materials as anti-frosting coating for condenser tubes will be further experimentally investigated. Therefore, the performance of the frost distribution on the surface will be considered in the next study.

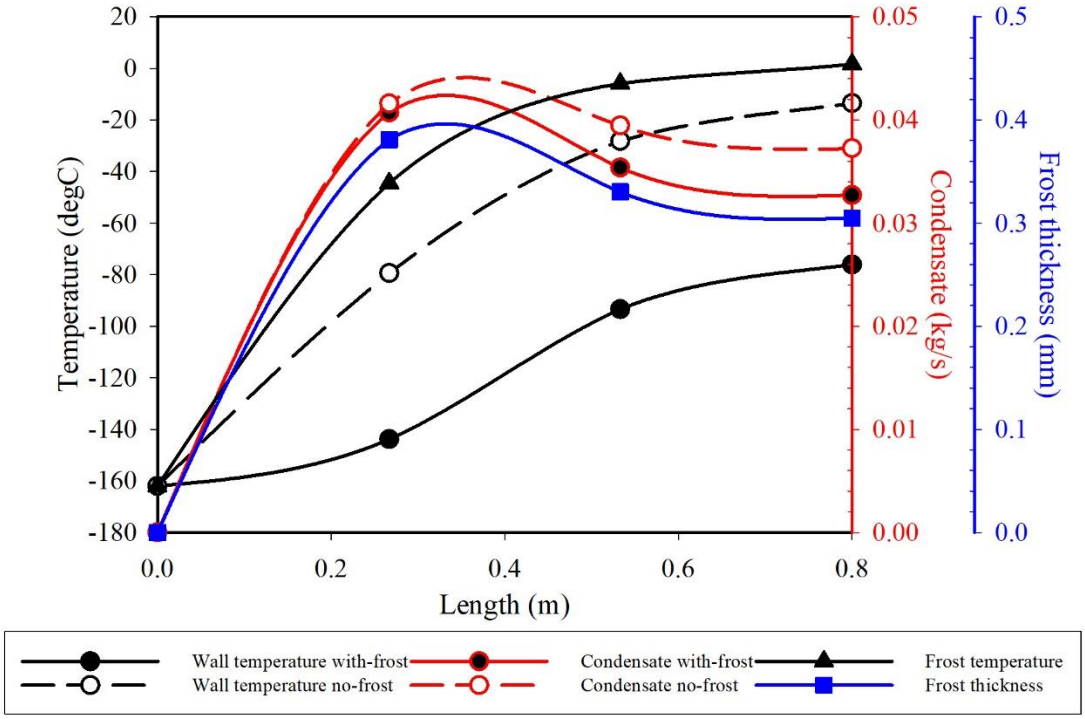

Fig. 15. Comparison between with-frost model and no-frost model.

4.4 Comparative analysis

As previously discussed, the FWG system is an essential facility for marine applications. In this section, the performance of the proposed optimised system is employed for a cruise ferry with a service speed of 22 knots and utilizing a DF-Electric power plant. This ferry is operated on the route Stockholm to Finland for 48 hours (including 5 hours harbour time) with two-way voyage and one intermediate stop. The LNG on this ferry is operated from the tank at temperature of -138 ℃ and 5 bar pressure. During the 48 hours, the NG consumption is varying from 0.17 kg/s to 0.88 kg/s in red solid line of Fig. 16. The feed-in seawater enters the vacuum evaporator of FWG under 0.08 bar, then the evaporated water vapour is condensed by the LNG cryogenic energy released from the LNG vaporization. Considering the FWG manual, the LNG pipeline and simulation results, the FWG is optimised in a volume of 0.5 m^3, in which the condenser is designed as a 3 passes compact heat exchanger with the effective heat exchanger area of 47 m^2. The calculated freshwater production of the proposed single-stage FWG varies with time in the 48-hour voyage time is presented as the black solid line in Fig. 16. The total freshwater production rate in 48 hours is 16991 kg with the LNG cryogenic energy consumption varying from 212 kW to 973 kW during LNG regasification process on board.

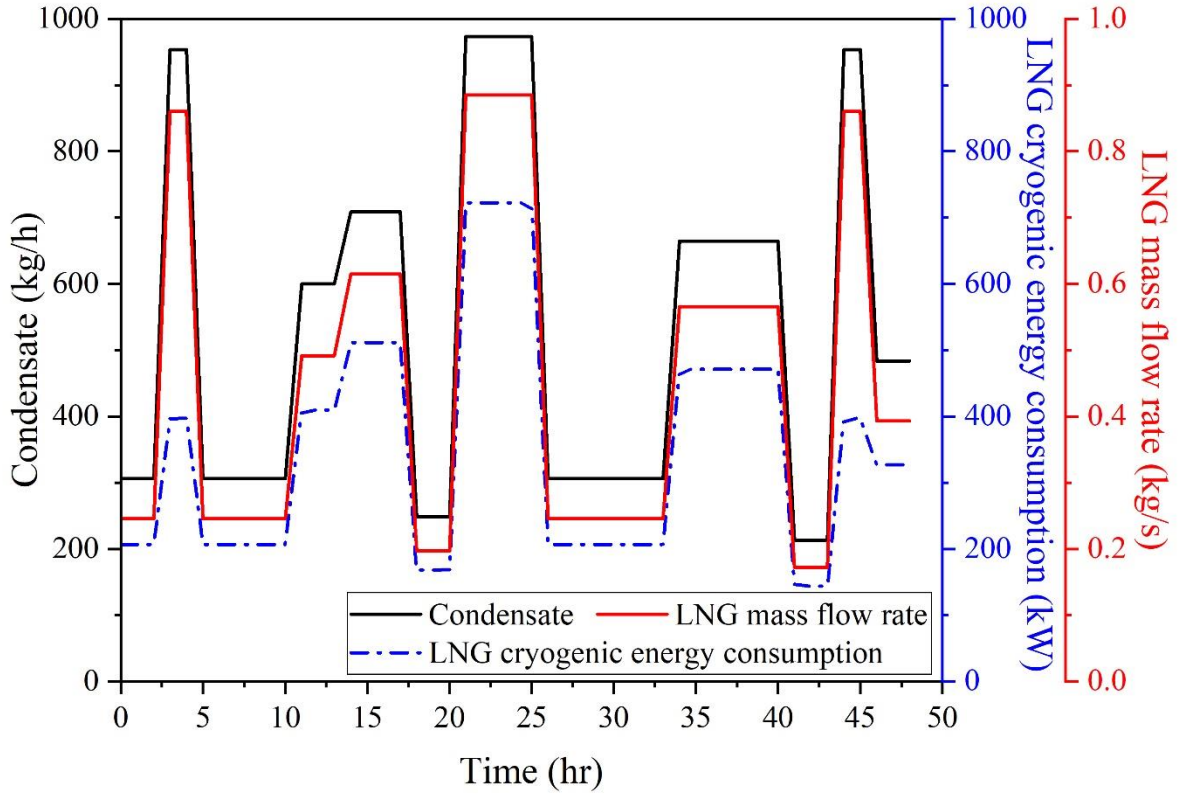

Fig. 16. The LNG cryogenic energy condition on the cruise ferry [49].

Consequently, the proposed optimal FWG system is feasible for marine applications of varying operational conditions. The LNG outlet temperature under all the operation conditions is lower than the required temperature for the engine of 27 ℃. Therefore, there is still extra LNG cryogenic energy available which can be utilized for other uses on board, i.e., air-conditioning system and cold storage system. Furthermore, this single-stage FWG system also has the potential to be utilized with the LNG terminal on land. The increased amount of LNG cryogenic energy in the LNG terminal can be expected to produce much more freshwater for land-based industrial and domestic use.

Based on the parametric analysis above, the optimisation of the FWG system mainly lies on feed-in water condition, cooling medium condition and the condenser configuration. In order to improve the freshwater production rate, feed-in seawater needs to be close to saturation temperature under specific vacuum pressure and with an optimal mass flowrate. Cooling medium is ideal to be low temperature and with a higher mass flowrate, which would be decided in terms of the specific LNG regasification flowrate on a vessel or a receiving terminal. It is expected that the evaporator can be heated by low-temperature cooling water on board a ship or other low temperature heat sources. The optimal convective exchange area of the condenser is design on the basis of the maximum available LNG cryogenic energy on a case ship. The major parameters of the proposed FWG system are listed in Table 6.

Table 6 Geometry and operational parameters of the proposed system.

Parameters	Unit	Quantity	Parameters	Unit	Quantity
Feed-in seawater temperature	℃	61.5	Thickness of the condenser wall	mm	0.265
Feed-in seawater mass flow rate	kg/s	0.36	Material of the condenser	-	Al Alloy 3003-H14
Pressure of the chamber	bar	0.08	Heat exchange area of the condenser	m^2	47.04

LNG mass flow rate	kg/s	0.875	Characteristic length of the condenser	mm	6
LNG temperature	℃	-162, -138	Heating input capacity of the evaporator	kW	770

In Table 7, freshwater production, RR and GOR of the proposed system are compared with the thermal desalination technologies and the other desalination technologies, e.g. HDH, FD, respectively. With the feed-in water mass flow rate of 1296 kg/h, LNG mass flow rate of 3150 kg/h and temperature of -162 ℃, the freshwater production is 1021.7 kg/h while the RR and GOR reaching 79% and 0.90. Compared with the normal cooling water as the working fluid in the condenser, the heat absorbed by the cooling water is less than the lower temperature LNG, which results in less water production rate and lower GOR. The freshwater production and the GOR of the LNG assisted FWG are around 7 times more than the normal FWG with cooling water of 5 ℃ in the condenser.

The exergy performance of the system is calculated as the ratio of the output freshwater exergy to the input exergy of each component. The input exergy of the evaporator and condenser is 95.5 kW and 958 kW, consisting of the input feed-in seawater exergy, input heating exergy, input LNG exergy and the pump exergy. Therefore, according to Eq. (25), the EPR of the whole FWG system is 8.17%.

Table 7 Comparison between the proposed system with other desalination technologies.

Method	Ref.	Description	Maximum freshwater production	RR	GOR	EPR
FD	Lin, et al. [25]	An indirect-contact FD method with the refrigerant R410A as the intermediate fluid and LNG as the cryogenic fluid with the following conditions: seawater with salinity of 2.36% and temperature of 5 ℃ and R410 A with the temperature of -18.2 ℃.	190.9 kg/h	42.2%	-	-
	Chang, et al. [50]	An indirect contact FD using EG as coolant and R23 as LNG to lower the temperature of EG.	0.52-0.55 kg/h	26%	-	-
HDH	Tariq, et al. [1]	An innovative HDH integrated with solar collector and air saturator with the air temperature of 25 ℃, absolute humidity of 11.2 g/kg and mass flow rate of 0.05 kg/s.	18 kg/day	7%-60%	0.35-0.75	-
	Deniz and Çınar [32]	A peformance analysis study on an HDH using solar energy and photovoltaic system is proposed during July in Turkey.	10.87 L/day	-	0.97	0.03%-1.87%
	Faegh and Shafii [51]	An HDH assisted by a heat pump cycle with an evaporation temperature of 40℃, condensation temperature of 8 ℃ and humidifier effectiveness of 0.85.	0.91 kg/h	1.3%	2.476	-
	Faegh and Shafii [4]	An evaporative condenser designed as a heater, humidifier and condenser in a heat pump integrated HDH system.	1.08 kg/h	-	2.00	-
Membrane-FD	Ahmad, et al. [27]	A hybrid RO-Freeze process using suspension crystallization to generate clean ice from the discarded two-stage RO brines.	135.87 t/year	56.8%	-	-
	Wang and Chung [26]	A hybrid desalination system comprising ICFD and DCMD intensified by LNG with the feed water of 8 kg, 3.5 wt%.	5.72 kg	71.5%	-	-
SCD	Kumar, et al. [19]	Possibility of ocean thermal gradient utilization in SCD which use surface seawater as the feed and deep seawater as the coolant at 5-10 ℃	5 kg/h	-	-	-

	Chen, et al. [52]	The spray evaporation process assisted by solar collector with an area of 7.6 m^2.	30 L/day	0.5%	0.80	-
SCD-Solar distillation	Mahkamov, et al. [53]	A solar distillation system with an area of 2.250 m^2 solar collector.	1.6 kg/h	-	-	-
SCD-FWG	Yuksel, et al. [6]	An optimisation study of FWG system using the Taguchi method to improve the freshwater recovery rate by 5.06%.	1069 kg/h	1.82%	-	-
	Morsy and Othman [5]	The waste heat recovered from scavenging air to provide heat for evaporator in FWG is proposed to supply 8 t/day freshwater.	8 t/day	7.78%	-	-
SCD-FWG-LNG	Current study	A thermal distillation type of FWG on board intensified by LNG cryogenic energy with the feed seawater of 61.5 ℃ and 0.36 kg/s.	1021.7 kg/h	79%	0.90	8.17%
	Current study on board	FWG-LNG applied on a cruise ferry kg with the LNG cryogenic energy consumption varying from 212 kW to 973 kW	16991 kg	79%	0.90	-

5. Conclusions

The innovative LNG cryogenic energy assisted thermal distillation technology is proposed in the paper. The Freshwater Generator (FWG) system using the technology is modelled with Siemens LMS Imagine. Lab Amesim. The system consists of the evaporation chamber, the condenser, the feed-in seawater tank, the LNG tank, vacuum pumps and pipework. The novelty of this work lies on the development of the condensation process assisted by the ultra-low temperature cooling medium: LNG. The validation models are first carried out under a series of experimental conditions in the literature. In order to explore the feasibility and the performance of the proposed FWG system, an overall model is developed to conduct sensitivity analysis for parameter optimisation, and a further scenario study on a case ship. The following conclusions can be drawn from the discussions:

1. The LNG cryogenic energy assisted FWG system is a reasonable way to produce freshwater on board. The experimentally validated evaporator and the condenser models are able to predict the production rate, the outlet temperature of LNG and required LNG cryogenic energy.
2. In the analysis, the pressure, the heating capacity, the feed-in seawater and cooling medium operation conditions have influences on the production rate. It is concluded that with a lower pressure, higher superheat and optimal mass flow rate, temperature and heating capacity, an increase in production will be achieved.
3. The configuration of the compact heat exchanger for condensation is analysed to obtain the optimal parameters for the proposed FWG system. The water production rate is correlated to the material properties, the heat exchange area with the variations of different geometry parameters, e.g., it has an inversely proportional relationship to the characteristic length of the heat exchanger.
4. The frost formation on the condenser surface presents different thickness distributions on different locations which will affect the condensate amount. And the details of this phenomena will be investigated in the future study.
5. The optimal LNG cryogenic energy intensified FWG system is able to provide freshwater supply of 1021.7 kg/h and exergy performance ratio of 8.17%.
6. Operating under conditions on the case ferry, this optimal FWG system is feasible to provide 16991 kg of freshwater for 48-hour voyage on board.

Appendix A Validation

A.1 Evaporator model

Rahman, et al. [35] proposed a single-effect desalination unit consisting of a submerged vertical tube evaporator and a cooling water tank. The submerged vertical tube evaporator is a shell and tube type heat exchanger with 175 tubes as shown in Fig. A- 1. Numerous tubes with a smaller diameter and shorter length are used rather than conventional long tubes. Feed-in seawater flows upward inside the vertical tubes from the feed water tank and is heated by hot water flowing outside the tubes. A series of experiments are designed to investigate the impact factors of the evaporation process, e.g. temperature, pressure, and flow rates of both feed-in and hot water in the evaporator chamber. The vapour production rate is the key indicator of the evaporator performance.

The operation parameters of the evaporator are presented in Table A- 1. In terms of the experimental results of the freshwater vapour production rate versus different superheat degrees, the evaporator model with the same parameters is built up. Fig. A- 2 illustrates a comparison between the simulated results and the experimental results of the freshwater vapour production rate in the evaporator with four different superheat degrees, i.e. 0 ℃, 5 ℃, 15 ℃, and 20 ℃. It is observed that the trend of the simulated water vapour production has a good agreement with the experimental data.

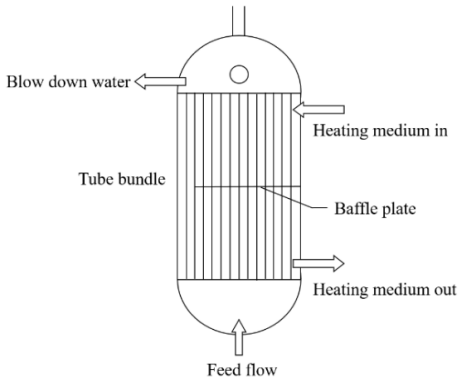

Fig. A- 1 The evaporator details in Rahman, et al. [35].

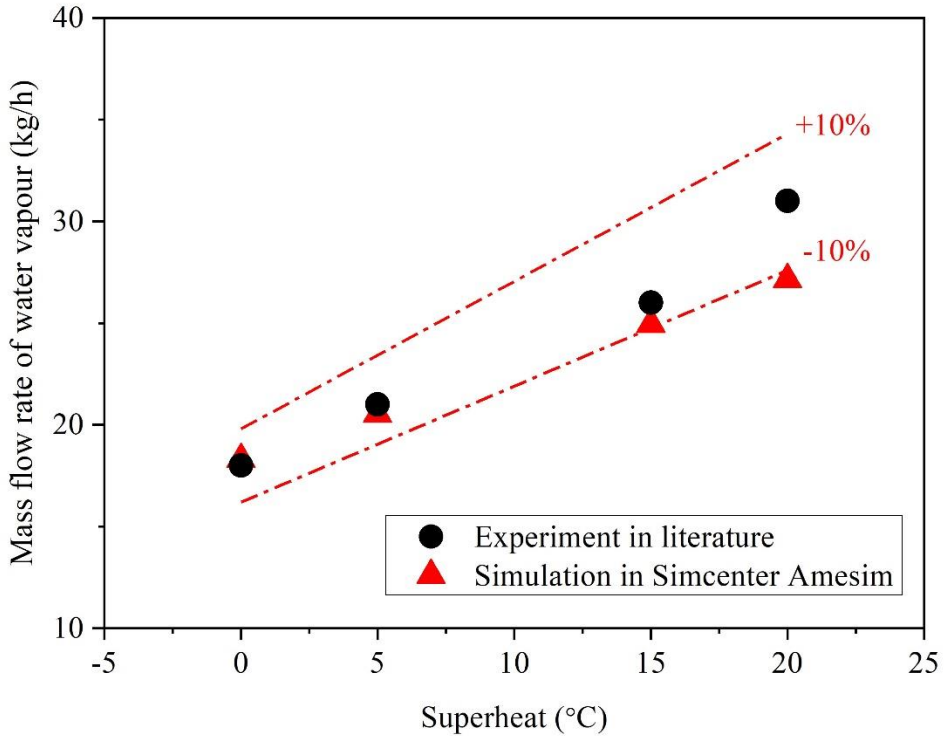

Fig. A- 2 Comparison between the measured and predicted in the evaporator model.

Table A- 1 Input parameters of the evaporator chamber for validation [35].

Parameter	Unit	Quantity
Volume of the chamber	L	31.416
Height of the chamber	mm	500
Initial percentage of liquid volume	-	0%
Temperature of inlet feed-in seawater	℃	41.5, 46.5, 56.5, 61.5
Mass flow rate of feed-in seawater	kg/s	0.0694
External heating medium capacity	W	12156
Initial pressure of the chamber	bar	0.08

A.2 Condenser model

To validate the accuracy of the condenser model developed in the Simcenter Amesim, the numerical results were compared with the experimental data conducted by Wu and Vierow [36] and Cheng and Geld [37]. The outlet temperature of the coolant and the condensate are widely-used parameters to predict the condensation performance. Wu and Vierow [36] explored the heat transfer characteristics of the condensation process on horizontal tubes. As shown in Fig. A- 3, the test section is a double pipe heat exchanger with the steam flowing inside the inner tube and coolant flowing outside in a counter direction. The condenser tube is made of SS304 in a heat transfer length of 3.0 m and an outer diameter of 31.7mm. The following input parameters in Table A- 2 are applied as two conditions, including inlet temperature, inlet humidity, mass flow rate and cooling water flow rate. Fig. A- 4 presents the simulated steam temperature profile at 4 different locations of tube: 0m, 0.5, 1.5m, 3m. It can be found that the numerical data agree very well with the experimental data. The errors between the numerical model results and the experimental data are within 7%.

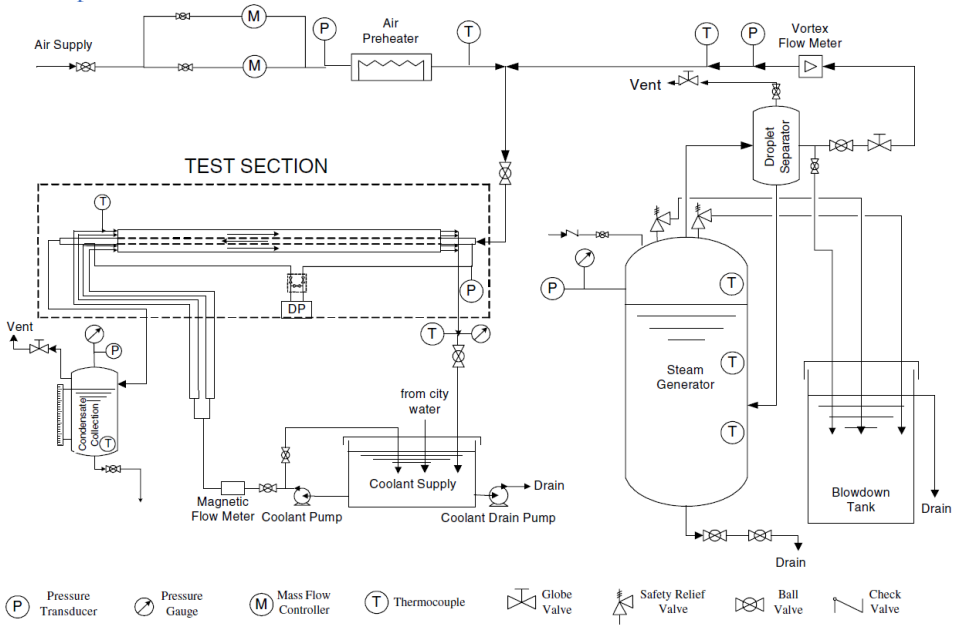

Fig. A- 3 Schematic of the test facility [36].

Table A- 2 Input operation parameters of the condenser for validation [36].

Parameter	Unit	Condition 1	Condition 2
Inlet temperature of air steam	℃	99	118
Air mass fraction	-	15%	15%
Absolute humidity	g/kg	5667	5667
Inlet steam flow rate	kg/s	0.007	0.012
Inlet temperature of the cooling water	℃	45	45

Flow rate of cooling water	kg/s	1.48	1.48
Pressure	bar	1	2

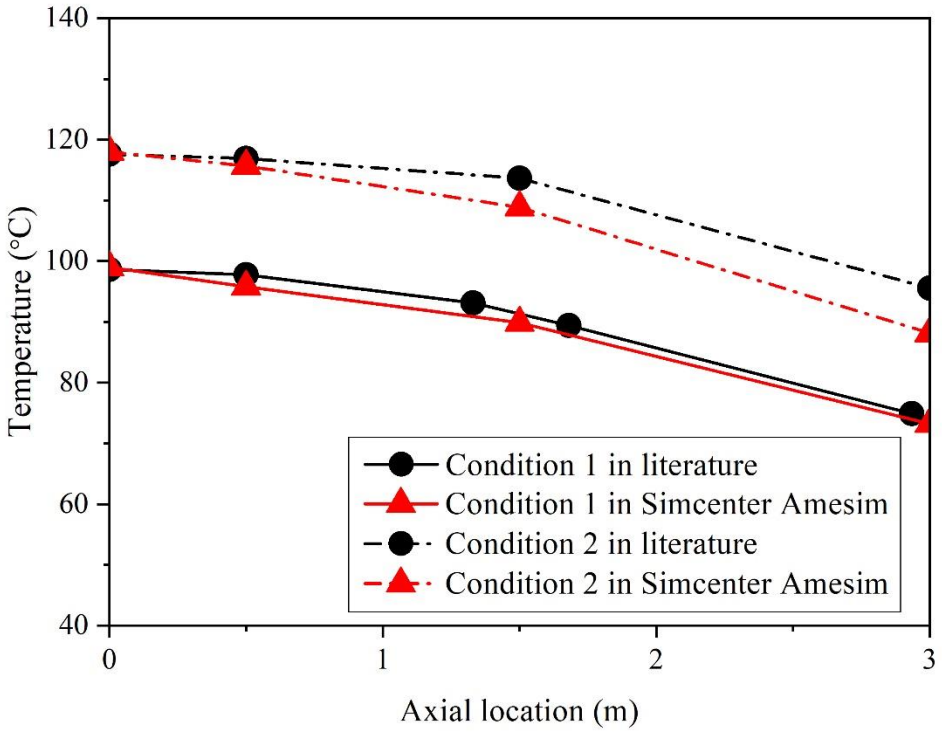

Fig. A- 4 Comparison between the measured and predicted in the condenser model.

A further condenser model validation is conducted to investigate if the quantity of condensate from the condenser model has a good agreement with the experimental results from Cheng and Geld [37]. The research group explored a compact polymer heat exchanger made of Poly-Vinyli-Dene-Fluoride (PVDF) for air steam-to-water heat exchange. As shown in Fig. A- 5, the heat exchanger consists of 48 parallel plates with 42 small cooling water channels in each plate. The steam supplied by a steam generator is mixed with the air together and then introduced into the condenser. The air-steam mixture enters the cross-flow parallel plate compact polymer heat exchanger to be condensed by the cooling water. The properties of PVDF is presented in Table A- 3. The input parameters in Table A- 4 are applied, including inlet temperature, inlet relative humidity, air-steam mass flow rate and cooling water flow rate, and the condensate mass flow is one of the outputs from experiments to validate the simulation results.

Table A- 3 Properties of PVDF (Poly-Vinyli-Dene-Fluoride) [54].

Parameter	Unit	Quantity
Density	kg/m^3	1780
Minimum temperature	℃	-62
Maximum temperature	℃	149
Specific heat	J/(kg·K)	1400
Thermal conductivity	W/(m·K)	0.2

Table A- 4 The condenser input parameters for validation [37].

Parameter	Unit	Quantity
Inlet temperature of air steam	℃	80, 90
Mass flow rate of air stream	kg/s	0.25 – 0.38
Relative humidity of air steam	-	20%, 24%, 32%, 40%

Inlet temperature of the cooling water	℃	25
Flow rate of cooling water	m^3/h	1.5, 2.5
Heat exchange area	m^2	1.4
Cross-sectional area of air stream side	mm^2	37600
Cross-sectional area of cooling water side	mm^2	2030
Pressure	bar	1
Duration time	s	1800

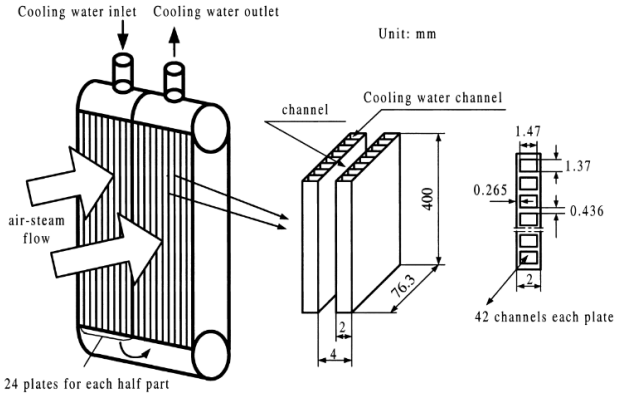

Fig. A- 5 Schematic of the polymer compact heat exchanger [37].

As shown in Fig. A- 6, the model predictions agree with the experimental data within -17.3% to +10%. It is observed that the simulated and calculated condensate mass flow rates have a gradually increasing difference when the condensate mass flow rate is greater than 0.009 kg/s. One of the reasons identified in the literature [37] is that it was very difficult to set the real testing parameters exactly the same as those set in the test plan table, which leads to the inaccuracy. The freshwater produced in the same duration time in the experiments also needs extra time to collect in full. Another possible reason is that the assumptions made in the validation model may ignore some factors affecting experimental results, e.g. the existence of non-condensable gases in the condenser, the imperfectness of the sealed testing system, etc.

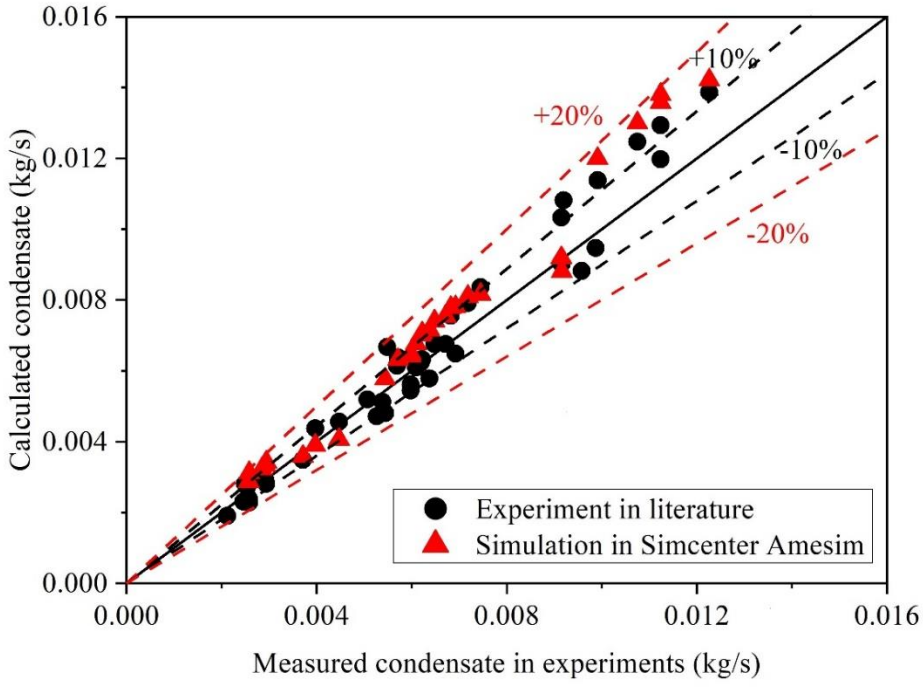

Fig. A- 6 Comparison between the measured and predicted in the condenser model.

Fig. A- 7 shows the comparison between the experimental and calculated frost layer thickness every 10 min during the 100-min test. It can be seen that the calculation based on the proposed frost formation model agree well with the experimental data. The relative error was about 29% with the rear part and 6% with the front part. The experiments investigated by Lee and Ro [38] present different frost layer thickness with different locations of the surface according to the non-uniform heat and mass transfer while this study simply assumes a uniform frost formation across the whole tube surface.

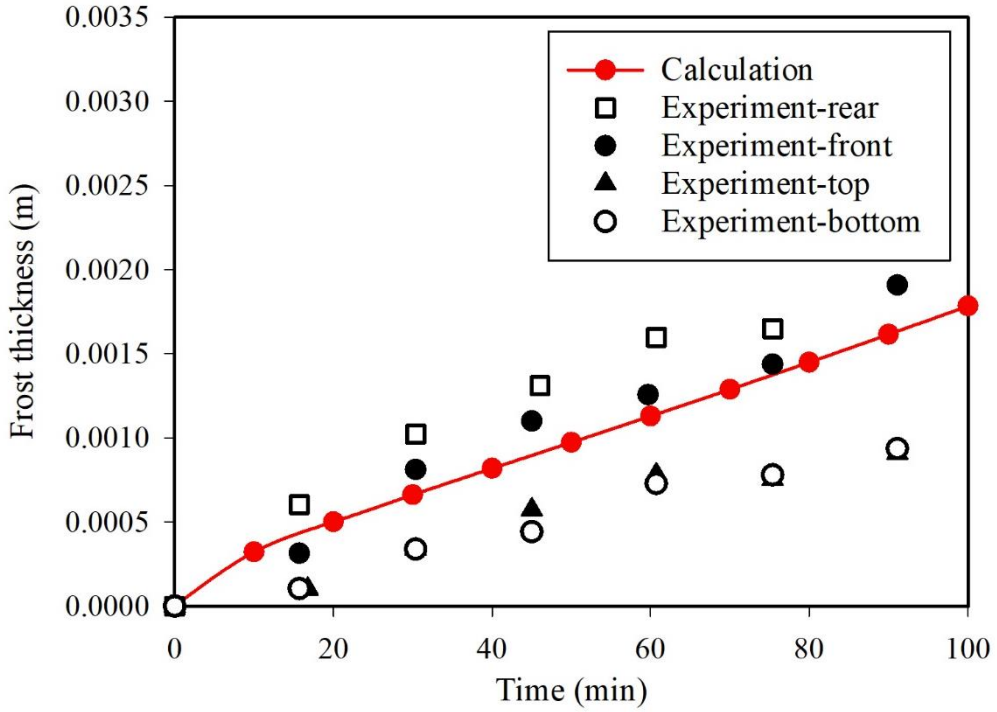

Fig. A- 7 Comparison between experimental and calculated frost layer thickness.

Appendix B

In this study, the properties of the three materials of the condenser: PVDF, Aluminium Alloy 3003-H14 and stainless steel AISI347 are summarized in Table B- 1.

Table B- 1 Material properties.

Properties	***Unit***	***PVDF [54]***	***Aluminium Alloy 3003-H14 [55]***	***Stainless Steel AISI347 [56]***
Density	*kg/m^3*	*1780*	*2730*	*8000*
Thermal conductivity	*W/ (m · K)*	*0.2*	*159*	*16.2*
Specific heat capacity	*J/ (kg · K)*	*1400*	*8930*	*500*
Ultimate tensile strength at -100℃	*MPa*	*-*	*175*	*690*
Elongation at break at -100℃	*-*	*-*	*19%*	*40%*
Coefficient of linear thermal expansion	*K^{-1}*	*1.2-1.4×10^{-4}*	*2.3×10^{-5}*	*1.73×10^{-5}*

Acknowledgement

The authors thank for the financial support from the UK EPSRC (Engineering and Physical Sciences Research Council) through the research project (EP/S00193X/2).

Reference

[1] R. Tariq, N.A. Sheikh, J. Xamán, A. Bassam, An innovative air saturator for humidification-dehumidification desalination application, Applied Energy, 228 (2018) 789-807.

[2] A. Al-Karaghouli, L.L. Kazmerski, Energy consumption and water production cost of conventional and renewable-energy-powered desalination processes, Renewable and Sustainable Energy Reviews, 24 (2013) 343-356.

[3] P. Tewari, R. Verma, B. Misra, H. Sadhulkan, Fresh water generators onboard a floating platform, in, 1997.

[4] M. Faegh, M.B. Shafii, Thermal performance assessment of an evaporative condenser-based combined heat pump and humidification-dehumidification desalination system, Desalination, 496 (2020) 114733.

[5] M. Morsy, H.H. Othman, Improving Green Fresh Water Supply in Passengers Ships Using Waste Energy Recovery, Journal of King Abdulaziz University: Marine Sciences, 21 (2010).

[6] O. Yuksel, Y. Gulmez, O. Konur, S.A. Korkmaz, A. Erdogan, C.O. Colpan, Performance assessment of a marine freshwater generator through exergetic optimization, Journal of Cleaner Production, 219 (2019) 326-335.

[7] S.S. Shenvi, A.M. Isloor, A. Ismail, A review on RO membrane technology: Developments and challenges, Desalination, 368 (2015) 10-26.

[8] P. Wagner, Desalination system of sea water for ship, in, Google Patents, 2002.

[9] A.D. Khawaji, I.K. Kutubkhanah, J.-M. Wie, Advances in seawater desalination technologies, Desalination, 221 (2008) 47-69.

[10] Y. Shao, Y. Li, L. Yang, X. Zhang, L. Yang, H. Wu, R. Xu, New experimental system for high pressure and high temperature flashing evaporation experiments, Applied Thermal Engineering, 66 (2014) 148-155.

[11] D. Saury, S. Harmand, M. Siroux, Experimental study of flash evaporation of a water film, International Journal of Heat and Mass Transfer, 45 (2002) 3447-3457.

[12] A.K. El-Fiqi, N. Ali, H. El-Dessouky, H. Fath, M. El-Hefni, Flash evaporation in a superheated water liquid jet, Desalination, 206 (2007) 311-321.

[13] M.J. Abbaspour, M. Faegh, M.B. Shafii, Experimental examination of a natural vacuum desalination system integrated with evacuated tube collectors, Desalination, 467 (2019) 79-85.

[14] F. Fathinia, M. Khiadani, Y.M. Al-Abdeli, A. Shafieian, Performance improvement of spray flash evaporation desalination systems using multiple nozzle arrangement, Applied Thermal Engineering, 163 (2019) 114385.

[15] O. Miyatake, T. Tomimura, Y. Ide, T. Fujii, An experimental study of spray flash evaporation, Desalination, 36 (1981) 113-128.

[16] Y. Ikegami, H. Sasaki, T. Gouda, H. Uehara, Experimental study on a spray flash desalination (influence of the direction of injection), Desalination, 194 (2006) 81-89.

[17] Q. Chen, Y. Li, K.J. Chua, Experimental and mathematical study of the spray flash evaporation phenomena, Applied Thermal Engineering, 130 (2018) 598-610.

[18] D.W. Meixi Liu, A new fresh water generation system under high vacuum degrees intensified by LNG cryogenic energy, in: 10th International Conference on Applied Energy Hong Kong, 2018.

[19] R.S. Kumar, A. Mani, S. Kumaraswamy, Experimental studies on desalination system for ocean thermal energy utilisation, Desalination, 207 (2007) 1-8.

[20] B.B. Kanbur, L. Xiang, S. Dubey, F.H. Choo, F. Duan, Cold utilization systems of LNG: A review, Renewable and Sustainable Energy Reviews, 79 (2017) 1171-1188.

[21] G. Maring, M. Mintz, The rapidly improving US energy outlook: positive implications for transportation, Institute of Transportation Engineers. ITE Journal, 84 (2014) 41.

[22] O. Nilsen, LNG Regulatory Update, in: Best fuel of the future conference & study tour, LNG regulatory update, DNV GL, 2018.

[23] E.G. Cravalho, J.J. McGrath, W.M. Toscano, Thermodynamic analysis of the regasification of LNG for the desalination of sea water, Cryogenics, 17 (1977) 135-139.

[24] W. Cao, C. Beggs, I.M. Mujtaba, Theoretical approach of freeze seawater desalination on flake ice maker utilizing LNG cold energy, Desalination, 355 (2015) 22-32.

[25] W. Lin, M. Huang, A. Gu, A seawater freeze desalination prototype system utilizing LNG cold energy, International Journal of Hydrogen Energy, (2017).

[26] P. Wang, T.-S. Chung, A conceptual demonstration of freeze desalination–membrane distillation (FD–MD) hybrid desalination process utilizing liquefied natural gas (LNG) cold energy, Water research, 46 (2012) 4037-4052.

[27] M. Ahmad, D.L. Oatley-Radcliffe, P.M. Williams, Can a hybrid RO-Freeze process lead to sustainable water supplies?, Desalination, 431 (2018) 140-150.
[28] T. He, S.K. Nair, P. Babu, P. Linga, I.A. Karimi, A novel conceptual design of hydrate based desalination (HyDesal) process by utilizing LNG cold energy, Applied energy, 222 (2018) 13-24.
[29] Z.R. Chong, T. He, P. Babu, J.-n. Zheng, P. Linga, Economic evaluation of energy efficient hydrate based desalination utilizing cold energy from liquefied natural gas (LNG), Desalination, 463 (2019) 69-80.
[30] P. Babu, A. Nambiar, Z.R. Chong, N. Daraboina, M. Albeirutty, O.A. Bamaga, P. Linga, Hydrate-based desalination (HyDesal) process employing a novel prototype design, Chemical Engineering Science, 218 (2020) 115563.
[31] T.L. Bergman, F.P. Incropera, D.P. DeWitt, A.S. Lavine, Fundamentals of heat and mass transfer, John Wiley & Sons, 2011.
[32] E. Deniz, S. Çınar, Energy, exergy, economic and environmental (4E) analysis of a solar desalination system with humidification-dehumidification, Energy Conversion and Management, 126 (2016) 12-19.
[33] M.J. Moran, H.N. Shapiro, D.D. Boettner, M.B. Bailey, Fundamentals of engineering thermodynamics, John Wiley & Sons, 2010.
[34] T.H. Chilton, A.P. Colburn, Mass transfer (absorption) coefficients prediction from data on heat transfer and fluid friction, Industrial & engineering chemistry, 26 (1934) 1183-1187.
[35] H. Rahman, M.N.A. Hawlader, A. Malek, An experiment with a single-effect submerged vertical tube evaporator in multi-effect desalination, Desalination, 156 (2003) 91-100.
[36] T. Wu, K. Vierow, Local heat transfer measurements of steam/air mixtures in horizontal condenser tubes, International journal of heat and mass transfer, 49 (2006) 2491-2501.
[37] L. Cheng, C.W.V.D. Geld, Experimental study of heat transfer and pressure drop characteristics of air/water and air-steam/water heat exchange in a polymer compact heat exchanger, Heat transfer engineering, 26 (2005) 18-27.
[38] Y. Lee, S. Ro, An experimental study of frost formation on a horizontal cylinder under cross flow, International journal of refrigeration, 24 (2001) 468-474.
[39] Y. Lee, J. Park, C. Han, Modeling and analysis of frost growth in pilot-scale ambient air vaporizer, Industrial & Engineering Chemistry Research, 57 (2017) 5933-5943.
[40] S. Liu, W. Jiao, L. Ren, H. Wang, P. Zhang, Dynamic heat transfer analysis of liquefied natural gas ambient air vaporizer under frost conditions, Applied Thermal Engineering, 110 (2017) 999-1006.
[41] S. Nath, J.B. Boreyko, On localized vapor pressure gradients governing condensation and frost phenomena, Langmuir, 32 (2016) 8350-8365.
[42] P. Zhang, F. Lv, A review of the recent advances in superhydrophobic surfaces and the emerging energy-related applications, Energy, 82 (2015) 1068-1087.
[43] D.-Y. Ji, J.-W. Lee, W. Hwang, K.-Y. Lee, Experimental study of condensation heat transfer on a horizontal aluminum tube with superhydrophobic characteristic, International Journal of Heat and Mass Transfer, 134 (2019) 286-295.
[44] K.S. Boyina, A.J. Mahvi, S. Chavan, D. Park, K. Kumar, M. Lira, Y. Yu, A.A. Gunay, X. Wang, N. Miljkovic, Condensation frosting on meter-scale superhydrophobic and superhydrophilic heat exchangers, International Journal of Heat and Mass Transfer, 145 (2019) 118694.
[45] M.-H. Kim, D.R. Kim, K.-S. Lee, Stochastic approach to the anti-freezing behaviors of superhydrophobic surfaces, International Journal of Heat and Mass Transfer, 106 (2017) 841-846.
[46] M.-H. Kim, H. Kim, K.-S. Lee, D.R. Kim, Frosting characteristics on hydrophobic and superhydrophobic surfaces: A review, Energy Conversion and Management, 138 (2017) 1-11.
[47] Y. Lu, J. Song, X. Liu, W. Xu, Y. Xing, Z. Wei, Preparation of superoleophobic and superhydrophobic titanium surfaces via an environmentally friendly electrochemical etching method, ACS Sustainable Chemistry & Engineering, 1 (2012) 102-109.
[48] M.A. Rahman, A.M. Jacobi, Drainage of frost melt water from vertical brass surfaces with parallel microgrooves, International Journal of Heat and Mass Transfer, 55 (2012) 1596-1605.
[49] E.-L. Tsougranis, Utilising the thermal and cryogenic waste energy for LNG driven vessels, in: School of Marine Science and Technology, Newcastle University, 2018.
[50] J. Chang, J. Zuo, K.-J. Lu, T.-S. Chung, Freeze desalination of seawater using LNG cold energy, Water research, 102 (2016) 282-293.
[51] M. Faegh, M.B. Shafii, Performance evaluation of a novel compact humidification-dehumidification desalination system coupled with a heat pump for design and off-design conditions, Energy Conversion and Management, 194 (2019) 160-172.

[52] Q. Chen, M.K. Ja, Y. Li, K. Chua, Evaluation of a solar-powered spray-assisted low-temperature desalination technology, Applied energy, 211 (2018) 997-1008.
[53] K. Mahkamov, E. Orda, B. Belgasim, I. Makhkamova, A novel small dynamic solar thermal desalination plant with a fluid piston converter, Applied Energy, 156 (2015) 715-726.
[54] HOLSCOT, PVDF, in, https://holscot.com/glossary/pvdf/ [accessed 14 Jan 2019].
[55] Properties and Selection: Nonferrous Alloys and Special-Purpose Materials, in: Metals Handbook, ASM International 10th Ed, 1990.
[56] P.D. Harvey, Engineering Properties of Steels, American Society for Metals, Metals Park, (1982).